



Antimicrobial peptides selectively target malaria parasites by a cholesterol-dependent mechanism

Received for publication, October 14, 2024, and in revised form, February 2, 2025. Published, Papers in Press, February 17, 2025.
<https://doi.org/10.1016/j.jbc.2025.108298>

Edo Kiper^{1,‡}, Daniel Ben Hur^{1,‡}, Daniel Alfandari¹, Abel Cruz Camacho¹, Naiem Ahmad Wani¹, Gal David Efrat¹, Mattia I. Morandi², Moshe Goldsmith¹, Ron Rotkopf³, Roman Kamyshinsky⁴, Arunaditya Deshmukh⁵, Nur Elyza Binte Zulkifli⁵, Navid Asmari⁶, Marcos Penedo⁶, Georg Fantner⁶, Ziv Porat⁷, Ido Azuri³, Irit Rosenhek-Goldian⁴, Chetan E. Chitnis⁵, Yechiel Shai^{1,*}, and Neta Regev-Rudzki^{1,*}

From the ¹Faculty of Biochemistry, Department of Biomolecular Sciences, Weizmann Institute of Science, Rehovot, Israel; ²Institute of Organic Chemistry and Biochemistry of the Czech Academy of Science, Prague, Czech Republic; ³Bioinformatics Unit, Department of Life Sciences Core Facilities, Weizmann Institute of Science, Rehovot, Israel; ⁴Department of Chemical Research Support, Weizmann Institute of Science, Rehovot, Israel; ⁵Unité de Biologie de Plasmodium et Vaccins, Institut Pasteur, Université Paris Cité, Paris, France; ⁶École Polytechnique Fédérale de Lausanne, Laboratory for Bio- and Nano-Instrumentation, Lausanne, Switzerland; ⁷Department of Life Sciences Core Facilities, Weizmann Institute of Science, Rehovot, Israel

Reviewed by members of the JBC Editorial Board. Edited by Chris Whitfield

Hundreds of thousands die annually from malaria caused by *Plasmodium falciparum* (*Pf*), with the emergence of drug-resistant parasites hindering eradication efforts. Antimicrobial peptides (AMPs) are known for their ability to disrupt pathogen membranes without targeting specific receptors, thereby reducing the chance of drug resistance. However, their effectiveness and the biophysical mechanisms by which they target the intracellular parasite remain unexplored. Here, by using native and synthetic AMPs, we discovered a selective mechanism that underlies the antimalarial activity. Remarkably, the AMPs exclusively interact with *Pf*-infected red blood cells, disrupting the cytoskeletal network and reaching the enclosed parasites with correlation to their activity. Moreover, we showed that the unique feature of reduced cholesterol content in the membrane of the infected host makes *Pf*-infected red blood cells susceptible to AMPs. Overall, this work highlights the Achilles' heel of malaria parasite and demonstrates the power of AMPs as potential antimalarial drugs with reduced risk of resistance.

Plasmodium falciparum (*Pf*), the most virulent causative agent of human malaria, accounts for over 99.7% of all malaria cases in Africa and was responsible for ~600,000 deaths in 2022 only (1). Alarming, the rapid development of parasitic resistance to all the commercial antimalarial drugs raises the challenge of controlling malaria worldwide (2, 3).

The complex life cycle of *Pf* alternates between the human host and the female *Anopheles* mosquito vector (2, 4). The symptomatic phase of the disease begins when parasites migrate from the hepatocytes, the initial replication niche, and invade and replicate within mature red blood cells (RBCs) (4). During the blood stage, the intracellular parasite progresses

through ring, trophozoite, and schizont developmental stages in an asexual replication cycle lasting approximately 48 h (4). At the final asexual stage of the cycle, new daughter cells (merozoites) are formed, egress, and invade into host uninfected RBCs (uRBCs) (4).

While numerous antimalarial drugs exist, the ongoing necessity for the development of new therapeutic approaches persists (5), primarily attributed to the parasite's rapid resistance development to commercial drugs, including frontline treatments and combination therapies (2, 3). In addition, the use of some antimalarial drugs could lead to severe adverse effects, as in the case of primaquine (6).

Antimicrobial peptides (AMPs) play a crucial role in the innate immune system and serve as the initial responders in interactions with various pathogens (7, 8). While AMPs exhibit diversity in their lengths, sequences, and structures, most of them are short and include a combination of hydrophobic and positively charged residues (9–11). Many of these peptides are unstructured in aqueous solutions and adopt amphipathic α -helix or β -sheet structures upon partitioning into membrane environments, which is a prerequisite for their lytic activity (12). AMPs interact *via* their hydrophilic residues with the membrane surface of the pathogen (12). Upon reaching a critical accumulation level of AMPs, the membrane is permeabilized either by transient pore formation or membrane disintegration, leading to cell death (12). Notably, the interaction of AMP with pathogens is mediated by two common attributes of the pathogens' membrane: 1) Negatively charged outer membranal leaflet, compared with the zwitterionic membrane of mammalian cells (12) and 2) the lack of cholesterol in the membrane of many pathogens, compared with mammalian cells, reduces the lipid bilayers' rigidity and induces membrane perturbation by AMPs (13). Importantly, unlike conventional drugs that target specific molecules, the mode of action (MoA) of AMPs is nonreceptor mediated (NRM MoA) and relies on electrostatic interactions with the

[‡] These authors contributed equally to this work.

* For correspondence: Yechiel Shai, yechiel.shai@weizmann.ac.il; Neta Regev-Rudzki, neta.regev-rudzki@weizmann.ac.il.

Cholesterol-dependent mechanism of antimalarial peptides

pathogen's membrane, limiting the probability of evolving resistance (12).

Here, we set a system to robustly examine the anti-*Pf* activity of diverse groups of AMPs (14–21), specifically on a *de novo*-designed family of synthetic peptides containing lysine (K) and leucine (L) residues in the *D* and *L* configurations, D,L-KL, peptides (14, 15). These alterations in amino acid sequence with the L-to-D modification led to disruptions in the secondary structure and hydrophobicity of the peptides. Indeed, D,L-K₆L₉ peptides exhibit antibacterial and anticancer activity while producing low hemolytic activity (14, 15) in both *in vitro* and *in vivo* (22, 23). Moreover, when applied to clinically isolated bacteria, these peptides did not induce drug resistance development (15).

Here, we identified two *de novo*-designed AMPs belonging to the D,L-K₆L₉ family, Amp1D (14, 15) and Seg5D (14, 15), that inhibit *Pf* growth while showing low hemolytic activity on uRBCs. Remarkably, the two active peptides demonstrated exclusive and strong binding to the infected host RBCs, while showing no binding to uninfected, healthy RBCs. Monitoring the subcellular localization of the active peptide Amp1D within the infected RBC (iRBC) by imaging flow cytometry (IFC), we could visualize its insertion into the enclosed *Pf* cell, with accumulation in proximity to the parasitic nucleus. Subsequently, we directed our efforts to study the MoA of Amp1D, particularly investigating the mechanical properties of the treated host RBC membrane and cytoskeleton. Using atomic force microscopy (AFM) (24), we initially found that the rigidity of the peptide-treated *Pf*-iRBCs was significantly reduced. Moreover, AFM images combined with computer vision analysis (25) revealed that Amp1D severely damages the structure of the host RBC cytoskeleton network.

In order to identify the key membrane component (of the infected cell involved) that governs the peptide binding, we utilized large unilamellar vesicle (LUV) (26) models to compare the membrane composition of *Pf*-iRBCs versus uRBCs. We demonstrate that the reduced levels of cholesterol in the plasma membrane of *Pf*-infected cell play a critical role in both the affinity and specificity of peptide binding. Furthermore, employing an unbiased *in vivo* approach, we show that upon cholesterol depletion from uRBCs, the peptide now exhibits binding capability.

Overall, this study opens a new therapeutic avenue in the battle against malaria, addressing the pressing challenge of drug resistance. We demonstrate that *de novo*-designed AMPs, known for reduced likelihood of drug resistance development, could serve as a new platform in combating malaria. Moreover, the reduced cholesterol levels on the infected cell membrane suggest another potential avenue for antimalarial drug development.

Results

Synthetic *de novo*-designed AMPs inhibit malarial growth

It was previously shown that AMPs, comprised of lysine (K) and leucine (L) residues (KL) in both *D* and *L* enantiomer configurations (*D,L*), have therapeutic potential against

pathogens without hemolytic and cytotoxic effects (14, 15, 27). The advantage of using D,L-KL AMPs lies in their high efficacy in targeting pathogen membranes with the reduced likelihood of drug resistance development, for instance in the case of clinical isolated bacteria (15). Yet, AMPs are not intuitively a straightforward choice for combating malaria. This is mainly since during the asexual blood stage, the intracellular *Pf* parasite is enclosed within its host RBC and lacks direct contact with the extracellular environment. Hence, there is uncertainty about whether such peptides could penetrate the host cell and access the encapsulated parasite. However, as the membrane of *Pf*-iRBCs differs greatly from uRBC host cells (28–30), we decided to test the efficacy of established synthetic *de novo*-designed AMPs (proven to act against pathogens) in the context of *Pf* growth (Table 1). We screened nine synthetic AMPs (Table 1) to assess their effect on *Pf* (NF54 strain) growth in culture. Three peptides included in this screen, Amp1D (14, 15, 27, 31), Seg5D (14, 15, 27, 31), and Seg6D (14, 15, 27, 31), differ in the distribution of their positively charged lysine residues. While Amp1D has an even distribution of lysine residues, Seg6D and Seg5D have lysine residues clustered in the center and at the margins of the molecule, respectively (Table 1, Fig. 1B). The 4DK5L7 (32, 33) peptide is shorter, with 12 residues compared with the 15 residues in the other KL peptides on the list (Table 1). In addition, KL peptides with lysine residues were used to form a peptide bond with their ϵ -amino group, termed the isopeptide bond. These isopeptide bond-AMPs, Amp1EP, AmpEP9, and AmpEP10, were previously shown to inhibit Gram-positive and Gram-negative bacteria without causing cytotoxic effect (16, 17). Finally, we used the human AMP LL-37 (19, 20, 34, 35), MSI-78 (18) (Fig. 1B) (commercially known as pexiganan), MSIEP (16), an analog to MSI-78 with isopeptide lysine residues, and the toxic AMP Melittin as a control (Table 1).

All these peptides shared common characteristics, including the presence of hydrophobic amino acids and a net positive charge ranging from +5 to +10 (Table 1). Their molecular weights fell within a similar range (approximately spanning from 1450 to 4490 g/mol) (Table 1). However, the hydrophobic moment (μ H), which predicts an increase in the insertion of the AMP to the membrane, varied among the peptides (Table 1). The peptides were designed and structured using ChemDraw synthesized on rink-amide resin using a peptide synthesizer, purified, and assessed for purity *via* reverse phase-HPLC and characterized by MALDI-TOF mass spectrometry (Fig. S1).

To identify candidate peptides with anti-*Pf* activity, the AMPs (12.5 μ M) were incubated with trophozoite stage-synchronized *Pf* parasites for 24 h, and the growth inhibition effect was measured using flow cytometry (36) (Fig. S2, A and B). We found that Amp1D and Seg5D (D,L-K₆L₉ family (15)) and MSI-78 (18) (a synthetic analog of a natural peptide) (Table 1) significantly inhibited *Pf* growth, leading to a significant reduction in parasitemia levels (Fig. 1A) while exhibiting low hemolytic activity (18) 1 h post treatment (HPT) and 24 HPT (Fig. 1, A and C). The human AMP LL-37 exhibited potent anti-*Pf* activity, in accordance with previous reports

Table 1
Peptide designation and properties

Peptide designation	Sequence ^a	Length (aa)	Net charge	MW (g/mol)	Relative hydrophobicity (%ACN) ^b	μH^c	Origin
LL-37	LLGDFFRKSKEKIGKEFKRIV QRIKDFLRNLPRTES	37	+7	4490	70.2	0.521	<i>Homo sapiens</i>
4DK5L7	KLLLKLLKLLK	12	+6	1450	53	0.435	<i>de novo</i>
Amp1D	LKLLKLLKLLKLL	15	+7	1804	60.1	0.836	<i>de novo</i>
Seg5D	KKKLLLLLLLLKKK	15	+7	1804	58.5	0.191	<i>de novo</i>
Seg6D	LLLLK KK KKLLLL	15	+7	1804	63.2	0.257	<i>de novo</i>
MSI-78	GIGKFLK AKK FGKAFVKILKK	22	+10	2476	55.3	0.647	Analog of <i>Xenopus laevis</i> AMP
MSIEP	GIGKFLK AKK FGKAFVKILKK	22	+10	2476	37.5	0.674	Analog of <i>Xenopus laevis</i> AMP
Amp1EP	LKLLKLLKLLKLL	15	+7	1804	50	0.836	<i>de novo</i>
AmpEP9	LKLLKLLKLLKLL	15	+7	1804	53.8	0.836	<i>de novo</i>
AmpEP10	LKLLKLLKLLKLL	15	+7	1804	54.2	0.836	<i>de novo</i>
Melittin	GIGAVLKVLTTGLPALISWIKRKRQQ	27	+6	2845	66.4	0.394	<i>Apis mellifera</i>

^a Underlined amino acids are D-enantiomers. Bold and italic amino acids are involved in isopeptide bond formation. All the peptides were amidated on at their C terminus.

^b The reversed-phase HPLC retention time in the C18 column using a gradient of 10–90% ACN in ddH₂O for 40 min.

^c Hydrophobic moment (μH) (32).

(37) but also showed higher hemolytic activity, leading to the destruction of uRBCs (Fig. 1, A and C). This nonselective activity of LL-37 was previously reported (35). LL-37 was shown to efficiently bind both zwitterionic and negatively charged phospholipid membranes, unlike other AMPs that selectively bind only to negatively charged membranes (35).

In contrast, the analogs of Amp1D and MSI-78 (Amp1EP, AmpEP9, AmpEP10, and MSIEP) displayed low activity together with hemolytic effect (Fig. 1A). These data suggest that incorporating lysine residues in their isopeptide bond form resulted in loss of anti-*Pf* activity (Fig. 1A). Thus, the specific chemical and biophysical properties of the peptides rather than the amino acid sequence itself are crucial factors contributing to the potency of anti-*Pf*.

While Amp1D, LL-37, MSI-78, and Seg5D showed low hemolytic activity in uRBCs (Fig. 1, A, C and D), we were interested to evaluate if their anti-*Pf* activity stems from rapturing the *Pf*-iRBCs. Therefore, we exposed magnet-isolated *Pf*-iRBCs (38) to Amp1D, LL-37, MSI-78, and Seg5D for 1 h. Noticeably, while these AMPs exhibit low hemolytic activity in the presence of uRBCs, *Pf*-iRBCs were more susceptible to hemolysis (Fig. 1D). Furthermore, Amp1D showed the highest hemolytic rate against *Pf*-iRBCs (Fig. 1D), suggesting that it is the most active anti-*Pf* AMP among the peptides we screened.

We then used a dose–response assay to evaluate the potency of the three leading active peptides, Amp1D, MSI-78, Seg5D as well as the human LL-37 peptide (Fig. 1E) on *Pf* growth. The half-maximal inhibitory concentration (IC₅₀) values were obtained after treating synchronized trophozoite-stage *Pf* cultures for 24 h. Amp1D exhibited the highest potency (IC₅₀ = 2.5 μM), followed by LL-37 (IC₅₀ = 9.0 μM), Seg5D (IC₅₀ = 9.0 μM), and MSI-78 (IC₅₀ = 10.2 μM) (Fig. 1E). The toxic peptide, Melittin, was used as a positive control (IC₅₀ = 0.921 μM) (Fig. 1E). Having established Amp1D as the most potent anti-*Pf* AMP, we aimed to determine its specific effect on the growth of either trophozoite-stage parasites or ring-stage parasites. Noticeably, trophozoite-stage parasites exhibited higher sensitivity to Amp1D, and their relative growth was reduced as compared with the ring-stage parasites (Fig. 1F).

Overall, these results indicate that the two peptides, Amp1D and Seg5D, exhibit significant anti-*Pf* activity while causing negligible damage to uRBC healthy human RBCs, suggesting a selective interaction with *Pf*-iRBCs.

Anti-*Pf* AMPs selectively bind to *Pf*-iRBCs

Next, we investigated the binding ability of Amp1D either to *Pf*-iRBCs (throughout the parasite blood stages: rings, trophozoites, and schizonts) or uRBCs, LL-37 was used as a control. In order to track the binding of these two peptides, the small fluorophore NBD (nitrobenzoxadiazole), which emits a fluorescent signal in a membranal environment (39), was conjugated to each peptide at the N terminus (31). Synchronized trophozoite-stage parasites were treated with either NBD-Amp1D or NBD-LL-37. The binding of the fluorescent peptides to *Pf*-iRBCs or uRBCs was monitored in time points throughout 24 h using flow cytometry (Figs. S1, S2, C–E and Table S2) as illustrated in Figure 2A. Remarkably, despite *Pf*-iRBCs constituting only about ~2% of the cells in the sample (*i.e.*, 2% parasitemia), NBD-Amp1D demonstrates significantly stronger binding selectivity to the infected cell and not to the uRBCs within the same sample, under both IC₅₀ and IC₂₅ concentrations (Figs. 2B and S3A).

Furthermore, within the population of the infected cells, we found that the interaction of the NBD-Amp1D to the host membrane reaches its peak selectivity binding at the late trophozoite–schizont stage, 8 HPT (Figs. 2B and S3A). In contrast, NBD-LL-37 demonstrated nonselective binding when compared between the two populations of infected and uninfected host cells (Figs. 2B and S3A). Similarly, two additional active anti-*Pf* AMPs, NBD-Seg5D and NBD-MSI-78, demonstrated preferred binding affinity to *Pf*-iRBCs in a similar trend to NBD-Amp1D (both at IC₅₀ and IC₂₅ concentration [Figs. 2D and S3A]).

Since the intensity of NBD signal was reported to be correlated with AMP activity (40), we further analyzed the flow cytometry binding data using the intensity signal data from NBD. Importantly, since each AMP molecule incorporates a single NBD

Cholesterol-dependent mechanism of antimalarial peptides

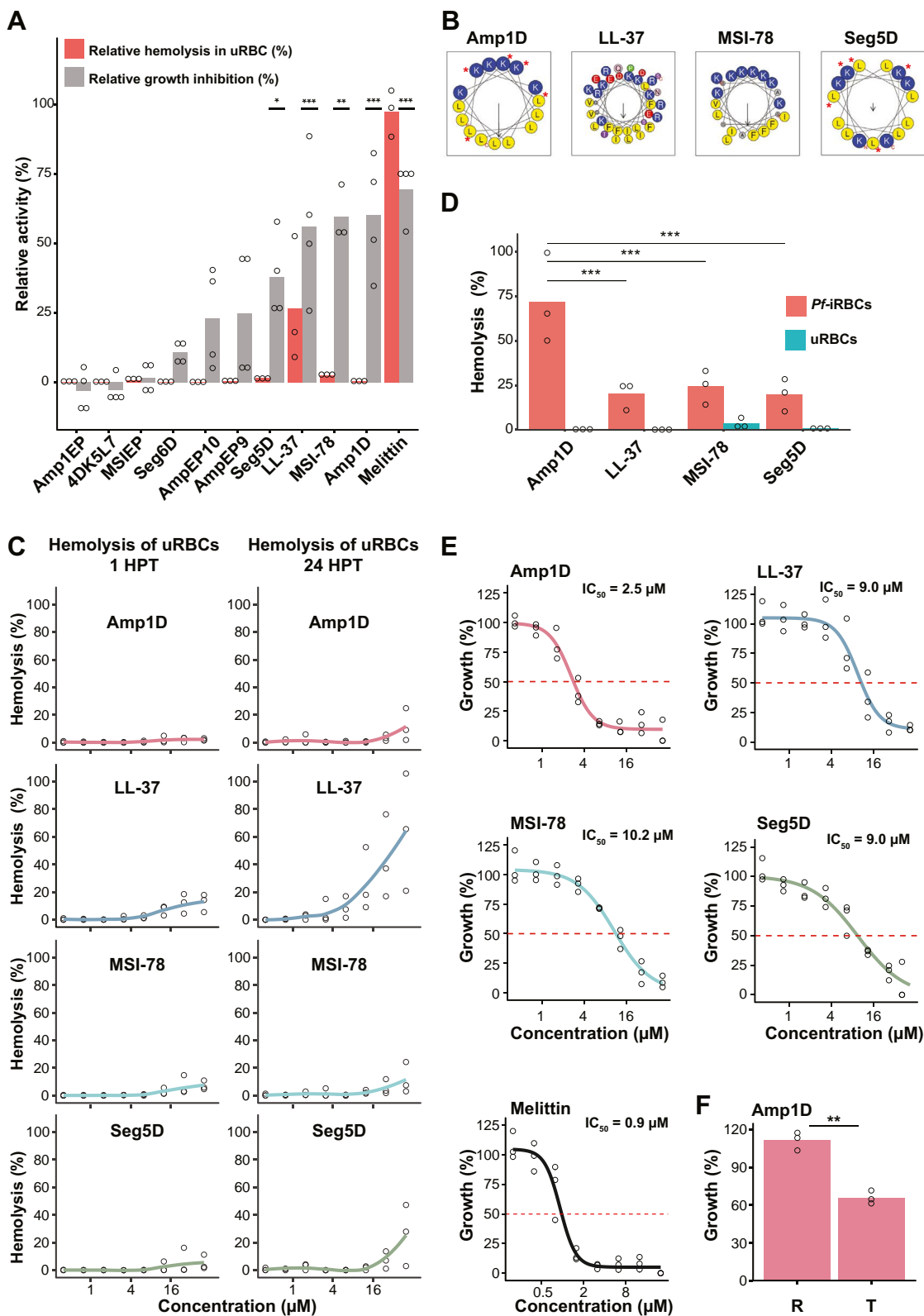


Figure 1. Synthetic *de novo*-designed AMPs demonstrate potent antimalarial activity and low cytotoxicity. A, trophozoite-stage parasites were incubated with 12.5 μM of the selected panel of AMPs (Table 1), and the relative growth of the parasites was measured 24 HPT (hours post treatment) using FACS (gray). uRBCs (uninfected RBCs) were incubated with 12.5 μM of the same AMP panel, and the relative hemolysis level was measured 24 HPT (red). Statistical analysis: Two-way ANOVA, with batch effect followed by a Dunnett's test $*p < 0.05$, $**p < 0.01$, and $***p < 0.001$. B, helical wheel projections of the four most potent AMPs. Positively charged residues are shown in blue, and negatively charged residues are shown in red. Hydrophobic residues are shown in yellow, polar uncharged amino acids are shown in purple, Gln amino acids is shown in pink, Gly and Ala aminoacids are shown in gray, and special residues are shown in green. The red asterisk (*) is an indication of the D-enantiomers. The helical wheel projections were generated in HeliQuest (60). C, relative hemolysis assay of uRBCs with a serial dilution of potent anti-Pf AMPs at 1 HPT and 24 HPT (N = 3). Hemolysis assay in C and growth assay in A were done in parallel. Thus, A and C share the same data for the measurement at 24 HPT and 12.5 μM for Amp1D, LL-37, MSI-78, and Seg5D. D, relative hemolysis

molecule, the signal intensity is a reliable proxy for the quantity of peptides bound to the cells (41), that is, the binding load (Figs. S2, C and D, and 2C). The analysis revealed that up to 4 HPT, the signal intensity of NBD-Amp1D was higher for *Pf*-iRBCs compared with the signal derived from the control uRBCs (Fig. 2C). The decrease in the binding intensity at 8 HPT of NBD-Amp1D (Fig. 2C) may be attributed to the dramatic transition of *Pf* stages from late trophozoites to early rings.

Indeed, these results correlate with the observed increase in the growth inhibition of trophozoite-stage parasite after exposure to Amp1D (Fig. 1E). The binding load of the control labeled peptide, NBD-LL-37, was not selective to between *Pf*-iRBCs and uRBCs (Fig. 2C), correlating with its lack of binding selectivity (Figs. 2B and S3A).

To determine the subcellular localization of the NBD-AMPs within *Pf*-iRBCs, we utilized IFC analysis (40, 42) for monitoring the active peptides, Amp1D, LL-37, Seg5D, and MSI-78 (Fig. 2D and S3B). We incubated the NBD-AMPs with synchronized trophozoite-stage parasites for 8 h, 4DK5L7 was used as inactive peptide control (Fig. 1A). In line with the binding selectively results of Amp1D (Fig. 2B), we detected a robust fluorescent signal in *Pf*-iRBCs treated with NBD-Amp1D both at IC₅₀ and IC₂₅ concentrations (Figs. 2D and S3B) but not in uRBCs (Fig. 2D). Interestingly, the signal from NBD-Amp1D was observed to be colocalized with the nucleus of the sealed parasite (Fig. 2D), similarly to the other active peptides (Seg5D and MSI-78, Fig. 1A) (Figs. 2D and S3B). In contrast, we could not detect a positive signal from the inactive peptide 4DK5L7 (Fig. 2D). These results suggest that the three active peptides can penetrate the plasma membrane of the infected host RBC and access the encapsulated parasitic cell. Oppositely, the detected signal for peptide NBD-LL-37 mainly appeared outside the cells, within small extracellular structures that are positive for DNA signal (Figs. 2D and S3B); this might suggest that those structures are postegress merozoites (Figs. 2D and S3B). However, higher resolution microscopy analysis is required to verify whether LL-37 binds to merozoite-stage parasites postegress from the *Pf*-iRBC.

To confirm the potential nuclear subcellular localization of Amp1D within *Pf*-iRBC, we labeled Amp1D using a Rhodamine fluorophore (Rho-Amp1D) (14, 27). The difference between rhodamine and NBD lies in the fact that rhodamine emits a fluorescent signal irrespective of membrane binding (14, 31). Notably, using IFC analysis, we could also visualize the accumulation of Rho-Amp1D signal in the region of the parasitic nucleus within the host cell (Fig. 2E). The signal intensity of Rho-Amp1D near the nucleus is stronger compared with regions external to the nucleus (Fig. 2F).

Together, these data suggest that Amp1D exclusively penetrates the multiple membranes of *Pf*-iRBCs, ultimately reaching the interior of the parasitic cell. Moreover, the

binding rate and intensity peaked during the late developmental blood stages (trophozoites–schizonts) (Figs. 2, B and C, and S3A) suggest that the peptide interaction may be driven by membranal alterations occurring in the infected cells during this stage of *Pf* development (43).

Amp1D peptide disrupts the membranal and cytoskeletal structure of the *Pf*-iRBC

To elucidate how Amp1D affects the biophysical properties of the *Pf*-iRBC, we used AFM to measure the structure and stiffness of the cells (24). We incubated Amp1D with synchronized trophozoite-stage parasites and analyzed the alterations in the cell stiffness, untreated cells were used as control. *Pf*-iRBCs were identified based on the presence or the absence of hemozoin pigment vacuole (44, 45) in bright field and by areas with higher Young's modulus containing parasites (Fig. 3A).

Although *Pf* is hidden within the host RBC, Amp1D induced exclusive structural changes in the membrane of *Pf*-iRBC. The mean sampled height values from treated *Pf*-iRBCs were lower compared with untreated *Pf*-iRBCs. In contrast, the control uRBCs did not show a similar response, exhibiting no significant changes in height upon Amp1D treatment (Fig. 3B). To further investigate the differences in the cell structure, we increased the resolution of the AFM scans by approximately four times (Figs. 3C and S4). Under our experimental conditions, uRBCs and *Pf*-iRBCs adhere to the surface with a round dome-like morphology (Figs. 3, A and C, and S4). Noticeably, upon exposure to Amp1D, *Pf*-iRBCs lost their characteristic round dome structure, and the membrane of the host RBC appeared to deflate and collapse (Figs. 3, A and C and S4). In contrast, untreated *Pf*-iRBCs maintain their round dome-like morphology (Figs. 3, A and C, and S4). These observed differences in the cell topography may indicate alterations in the membrane of the infected cell. Amp1D treatment could compromise the infected cell's ability to maintain its inflated dome-like shape, leading to a collapsed morphology around the parasite. In agreement with the change in the height of *Pf*-iRBCs, the mean Young's modulus of treated *Pf*-iRBCs was reduced compared with untreated *Pf*-iRBCs (Fig. 3D). While the measured modulus values obtained by this AFM-based method are influenced by all cell components, including cell membrane, bulk properties, and parasite properties, further investigation is necessary to ascertain which cell component is most affected.

The mechanical properties of RBCs are strongly influenced by the underlying cytoskeleton network (24, 46–48). Having established that the effect of Amp1D is restricted to *Pf*-iRBCs, we focused on studying the effect of Amp1D on the cytoskeleton structure of *Pf*-iRBCs (24). We isolated trophozoite-stage parasites using a magnetic column (38) (Fig. 4A, right) and treated them with Amp1D for 30 min. To expose the

assay for magnet-isolated *Pf*-iRBCs (at the trophozoite stage) and uRBCs using Amp1D, LL-37, MSI-78, and Seg5D after 1 HPT (N = 3), two-way ANOVA followed by Tukey's test, ****p* < 0.001. E, dose–response assay of the top four anti-*Pf* AMPs (Amp1D, MSI-78, LL-37, and Seg5D) and Melittin as a control. Trophozoite-stage *Pf* parasites were incubated with different AMPs at decreasing concentration levels, and the parasites' relative growth was measured 24 HPT. Statistical analysis of three biological replicates: IC₅₀ values were obtained using the package “*dr4pl*” for “R.” F, ring- and trophozoite-stage parasites were exposed to 3 h pulse of 5 μM Amp1D. The parasitemia was measured by flow cytometry after the next *Pf* invasion cycle. Growth (%) was measured after invasion of the treated ring- and trophozoite-stage parasites and was compared with untreated ring- and trophozoite-stage parasites, respectively. Statistical analysis: *t* test, **p* < 0.05, ***p* < 0.01 (N = 3). FACS, fluorescence-activated cell sorting. iRBC, infected RBC; *Pf*, *Plasmodium falciparum*.

Cholesterol-dependent mechanism of antimalarial peptides

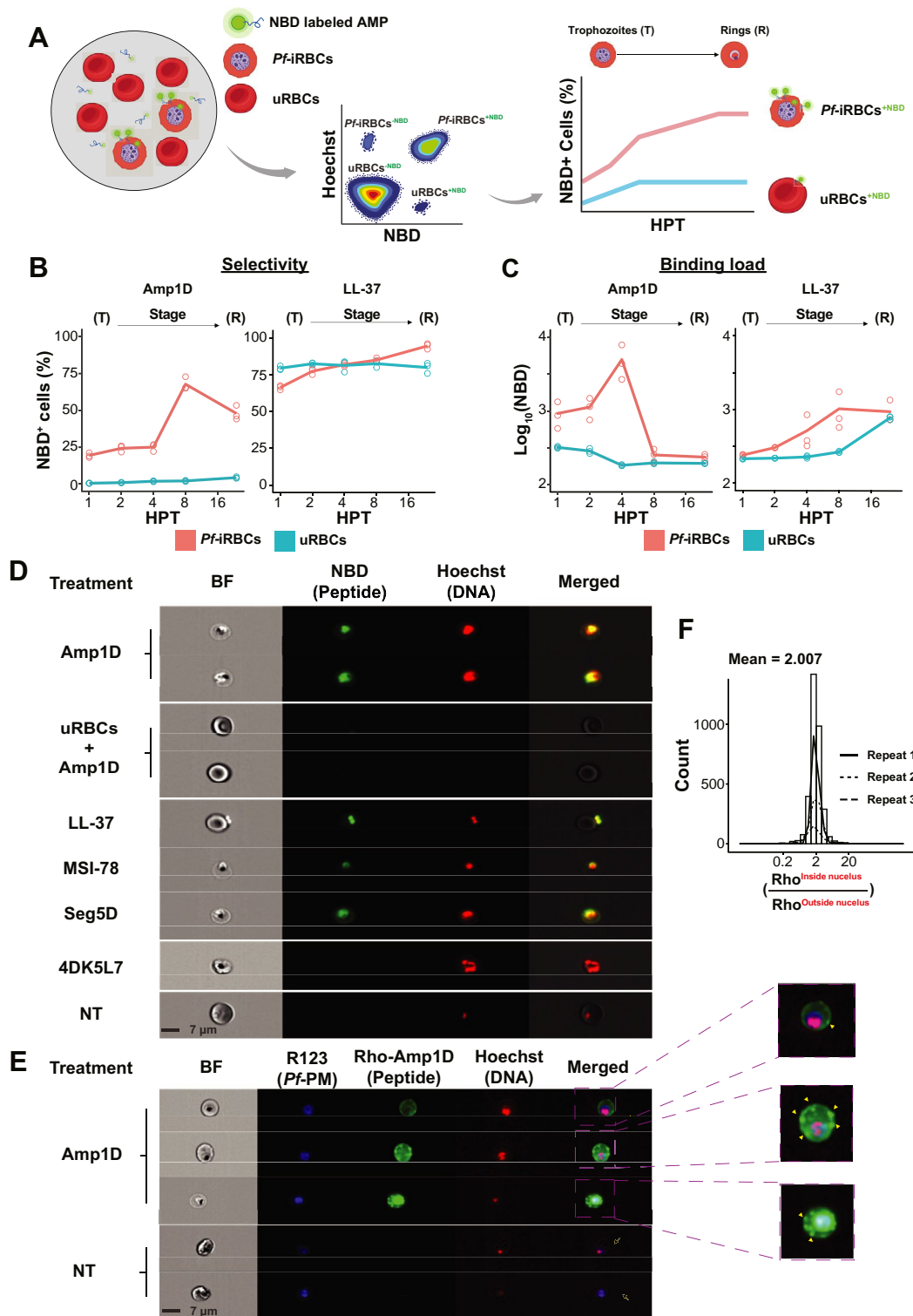


Figure 2. Anti-Pf AMPs selectively bind to Pf-iRBCs. A, An illustration of the experimental setup, including a representative schematic display of derived data. NBD-labeled peptides were incubated with a synchronized culture of 2% trophozoite-stage *Pf*. Using flow cytometry, we tracked the binding of the peptide and quantified the percentage of NBD⁺ uRBCs and Pf-iRBCs. B, binding selectivity assay (IC₅₀ concentrations) and (C) binding load analysis (IC₅₀ concentrations) of Amp1D, LL-37 (tagged with NBD fluorophore) to Pf-iRBCs (red) or uRBC analysis (blue). Trophozoite-stage parasites were incubated with the selected active NBD-AMPs for 24 h, and the binding selectivity and load were measured at five time points using flow cytometry. D, NBD-AMP interaction with Pf-iRBCs and uRBCs. Trophozoite-stage parasites were incubated with NBD-AMPs (IC₅₀) for 8 h, and images were obtained using imaging flow cytometry. Bright field (BF), NBD-AMP signal (green), DNA (Hoechst) (red), and merged channels are shown. E, IFC analysis for *Pf* parasites treated by Rho-Amp1D. Pf-iRBCs were isolated using magnetic column at the trophozoite stage. Parasites were incubated with Rho-Amp1D for 30 min. BF, *Pf* plasma membrane (Rhodamine 123 [R123], blue), Rho-Amp1D (green), DNA (Hoechst staining, red), and merged channels are shown. Yellow arrows indicate the accumulation of Rho-Amp1D on the membrane of Pf-iRBCs. F, IFC localization analysis of Rho-Amp1D. The ratio of the cosignals of Rho-Amp1D (corrected to area) with Hoechst-stained DNA (Rho^{Inside nucleus}) versus single signal of Rho-Amp1D (corrected to area), without Hoechst-stained DNA signal (Rho^{Outside nucleus}). iRBC, infected RBC; NBD, nitrobenzoxadiazole; *Pf*, *Plasmodium falciparum*; uRBC, uninfected RBC.

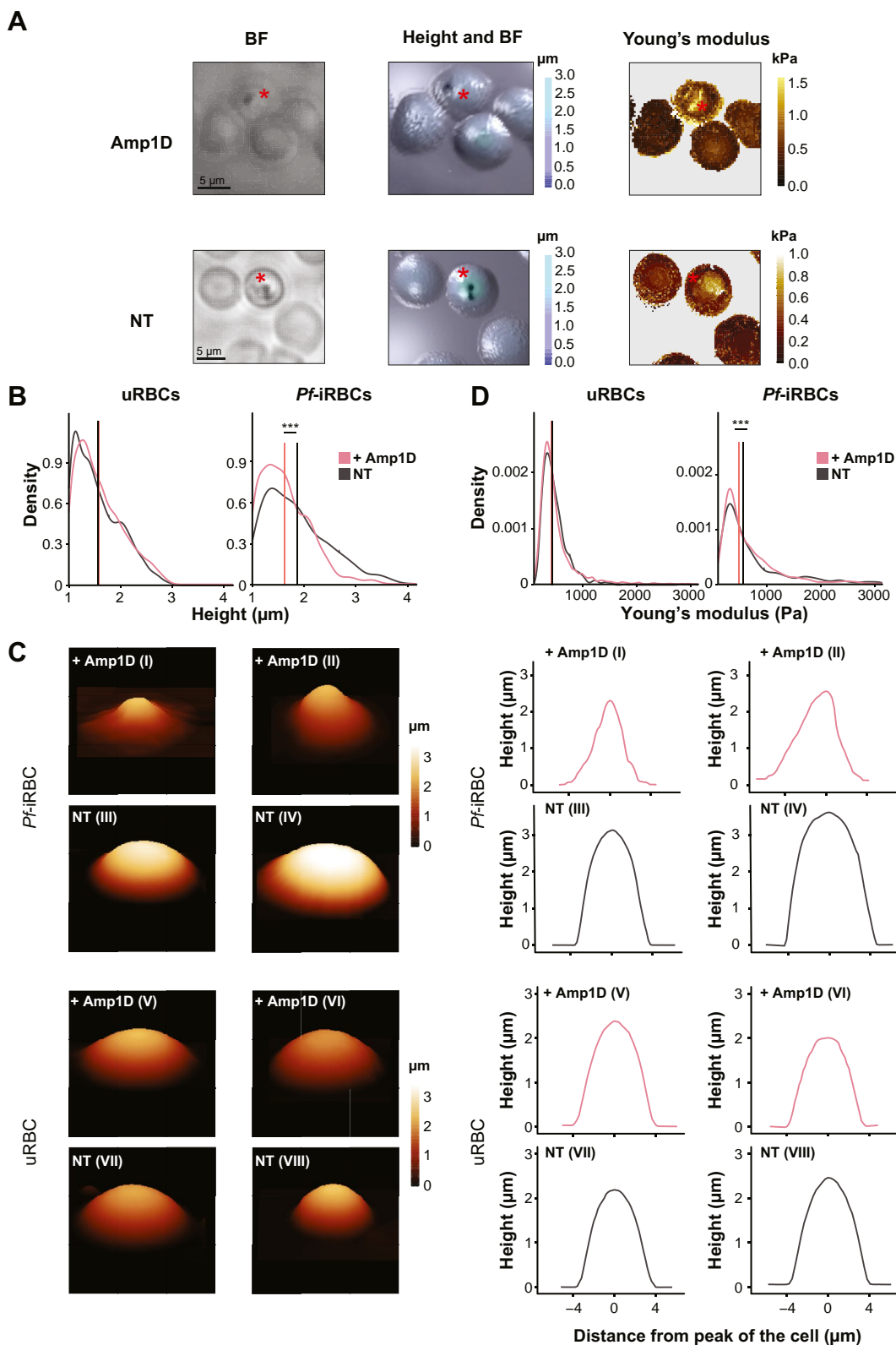


Figure 3. Amp1D induces structural and mechanical changes in Pf-iRBCs. A, a representative example of AFM maps of Pf-iRBCs marked with red asterisks and uRBCs. RBCs treated with (+Amp1D) or without (NT [nontreated]) treatment. AFM 3D topography map with bright field (BF) overlay, and the Young's modulus map of the cells are presented. B, comparison of the mean (vertical lines) height of total pixels from uRBCs and Pf-iRBCs with (+Amp1D, treatment for 2 h) or without (NT). C, left, representative 3D AFM-topography images of Pf-iRBCs and uRBCs with and without treatment of Amp1D (2 h). Right, a profile curve of the cells' height (from the images on the left). Roman numerals correlate the image of each cell and its height profile. D, comparison of the mean (vertical lines) Young's modulus of total pixels from uRBCs and Pf-iRBCs with (+Amp1D treatment for 2 h) or without (NT). Data represent three biological repeats. Statistical analysis was done using the packages "lmerTest" and "emmeans" for "R." The means were compared by two-way ANOVA with random batch effect analysis. *** $p < 0.001$. AFM, atomic force microscopy; iRBC, infected RBC; Pf, *Plasmodium falciparum*; uRBC, uninfected RBC.

Cholesterol-dependent mechanism of antimalarial peptides

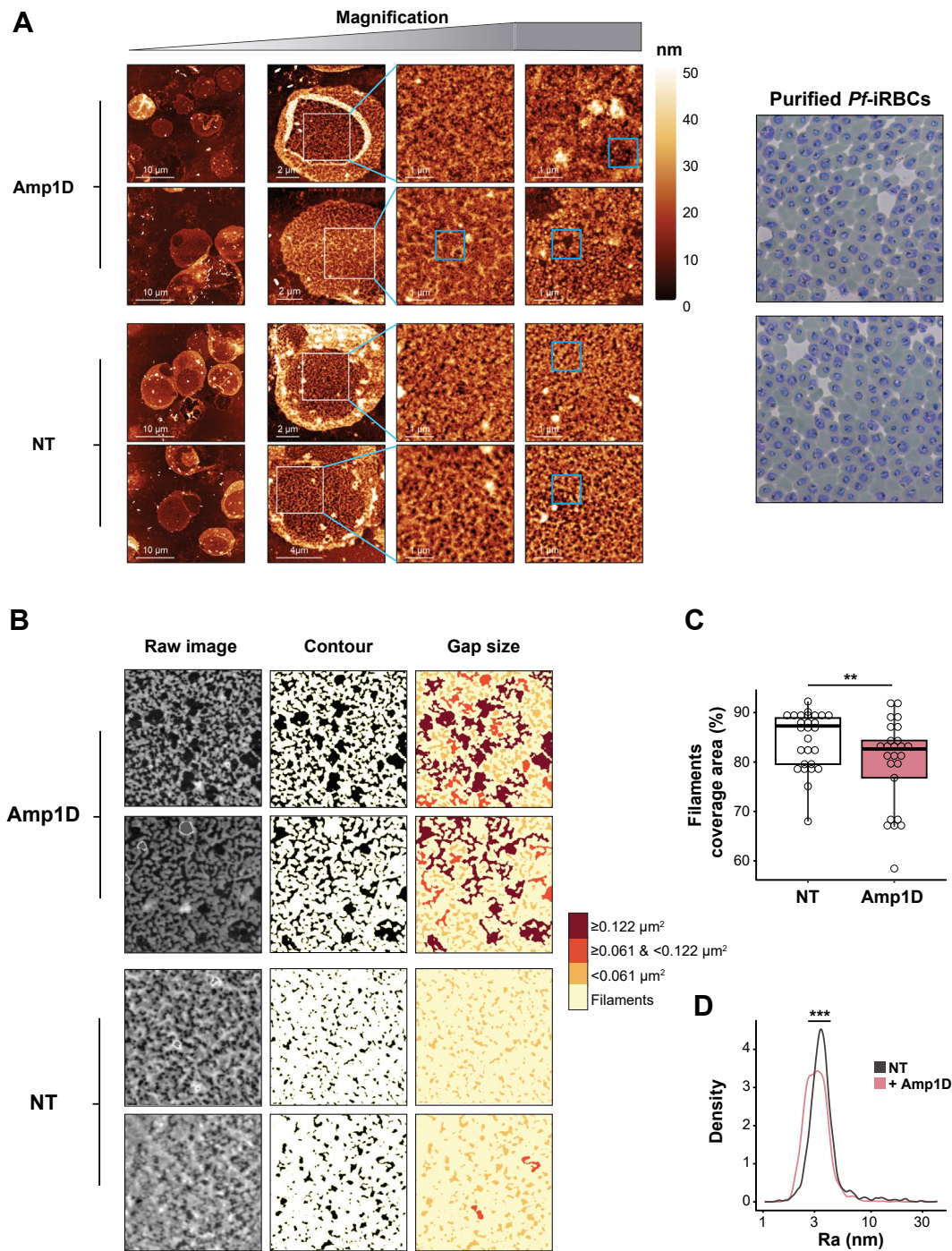


Figure 4. Amp1D disrupts the cytoskeleton structure of *Pf*-iRBCs. *A*, left, representative AFM images ($4 \mu\text{m} \times 4 \mu\text{m}$), in increasing magnification, of the cytoskeleton of *Pf*-iRBCs with (Amp1D) or without (NT [nontreated]), exposure to Amp1D for 30 min ($5 \mu\text{M}$) upon isolation *via* a magnetic column. *Blue boxes* represent an example of flattening of the filaments on the surface. *Right*, Giemsa-stained trophozoite-stage *Pf* parasites after separation using magnetic column. *B*, representative examples of the morphology analysis of *Pf*-iRBCs' cytoskeleton structure of *Pf*-iRBCs with (Amp1D) or without (NT) exposure to Amp1D for 30 min ($5 \mu\text{M}$) after isolation *via* a magnetic column. Raw images were processed to differentiate filaments from gaps and to calculate the percentage of area covered by the filaments and gaps. *C*, the area covered by filaments after treatment with Amp1D. Statistical analysis: two-Way ANOVA with random batch effect, $**p < 0.01$, each dot represents a cell, $N = 2$. *D*, the mean roughness of filaments after treatment with Amp1D. Statistical analysis: Mann–Whitney–Wilcoxon test: $***p < 0.001$. AFM, atomic force microscopy; iRBC, infected RBC; *Pf*, *Plasmodium falciparum*.

cytoskeleton of *Pf*-iRBCs treated or untreated, cells adsorbed onto poly-L-lysine-modified mica were washed with a hypotonic solution and then scanned in a dry state using AFM (Fig. 4A) (24). Images of $4 \mu\text{m} \times 4 \mu\text{m}$ were scanned in the center of each exposed cell cytoskeleton and used as an input

for the computer vision and image analysis pipeline. Notably, two significant structural phenotypic differences of the cytoskeleton were observed between the untreated and treated *Pf*-iRBCs (Fig. 4, A–D). First, each image was segmented to identify the backbone area (Fig. 4B), and the filament coverage

area was calculated in each image (Fig. 4C). It was found that the untreated *Pf*-iRBCs have a statistically significant higher percentage of area covered by filaments than the treated *Pf*-iRBCs. This leads to a lower coverage of filaments in the scanned area. Second, the mean roughness (Ra—profile height deviations from the mean line) was calculated on $0.5 \times 0.5 \mu\text{m}^2$ areas covered with a cytoskeleton network (Fig. 4D). The mean roughness was found to be larger in the untreated *Pf*-iRBCs in comparison to the treated cells, indicating that the filaments lost their structural height characteristics because of the treatment.

Overall, these results indicate that Amp1D reshapes the mechanical properties of *Pf*-iRBCs both at the membrane and cytoskeleton levels. Moreover, the exclusive interaction of Amp1D with *Pf*-iRBCs suggests that its selective MoA is likely dependent on specific membrane components.

Membranal cholesterol level determines the activity of Amp1D

Next, we sought to identify the key feature in the membrane of *Pf*-iRBCs that enhances the interaction of the peptides. AMP activity is positively correlated with reduced cholesterol and increasing negative charge in the membrane of pathogens (12, 49). In addition, it is known that *Pf* dramatically changes the host RBCs' membrane (50, 51) causing a reduction in cholesterol levels (50) as well as exposure of negatively charged phosphatidylserine (PS) lipids (51, 52). We therefore questioned whether the cholesterol and the PS modifications in the host membrane of the infected cell play a role in the selective binding of Amp1D. To address that and investigate the nature of the interactions between Amp1D and the host membrane, we utilized LUVs as a membranal model (26, 53). We used NBD-AMPs to measure their binding affinity to LUVs based on the ratio of lipids to peptide required to reach half maximal signal (K_d) (31).

In parallel, we monitored the change in NBD's emission spectra toward the blue edge of the spectrum (blue shift) to better understand its localization inside the hydrophobic lipidic core (39, 54–56). We then used a mixture of phosphatidylcholine (PC):cholesterol to model the membrane composition of uRBCs (57). The membrane of *Pf*-iRBCs is characterized with reduced level of cholesterol and higher level of PS (58, 59). Therefore, we synthesized LUVs comprised of only PC and a mix of PC and negatively charged PS (PC:PS). The affinity of the peptide for phospholipid membranes was assessed through titration of NBD-labeled peptide with LUVs (Fig. 5, A–C). Then, based on the emitted signal from the interaction of NBD-AMPs with the LUVs, we measured the affinity of the AMPs to different LUVs (K_d) (Figs. 5, A and C, and S5B) (31). The maximal fluorescence value (B_{max}) was used as a proxy to the binding load of the AMPs 4DK5L7, Amp1D, LL-37, Melittin, MSI-78, and Seg5D to the LUVs (31) (Fig. 5B).

We found that the presence of cholesterol in PC:cholesterol LUVs significantly reduced the binding affinity (K_d) of Amp1D, compared with LUVs with lacking cholesterol (PC and PC:PS LUVs) (Fig. 5A). These results were similar for the other active

peptides, Seg5D and MSI-78 (Fig. 5A). Notably, Melittin and LL-37, which have shown relatively higher hemolytic activity (Fig. 1, A and C), were less affected by the presence of cholesterol (Fig. 5A). Surprisingly, although Amp1D and other AMPs are positively charged, the additional negative charge in PC:PS LUVs did not improve the binding affinity (Fig. 5C). This indicates that the presence of cholesterol, rather than the absence of PS, inhibits the activity of AMPs. For LUVs composed with a combination of PC, PS, and cholesterol, the addition of PS increases AMP affinity as compared with PC:cholesterol LUVs (Figs. S5B and 5A). However, the affinity remained lower compared with the LUV with only PC (Figs. S5B and 5A). Further investigation is required to understand the interplay between PC, cholesterol, and PS on AMP–membrane interaction.

Previous reports indicated that binding load is a good predictor of AMP activity (31), possibly because of lower levels of peptide oligomerization (60, 61). Thus, we analyzed the maximal binding load of six NBD-labeled peptides (4DK5L7, Amp1D, LL-37, Melittin, MSI-78, and Seg5D) to LUVs by using the maximal emission, B_{max} , as an approximation. We detected a significant change in B_{max} level when AMPs were introduced to PC:cholesterol LUVs (Fig. 5B). The three peptides, Amp1D, Melittin, and LL-37, showed higher B_{max} levels than 4DK5L7 Seg5D and MSI-78 (Fig. 5B). These results suggest that AMPs may need to achieve a minimal binding load when encountering the membrane of the infected cell in order to act as an active anti-*Pf*.

We further investigated the localization of Amp1D, LL-37, Seg5D, MSI-78, 4DK5L7, and Melittin within the LUV using AMPs labeled at their N-terminal region (by the fluorescent probe NBD). Altered spectra of the fluorescence to the blue end of the spectrum (blue shift) upon exposure to LUVs indicate that the NBD group is relocated into the membrane hydrophobic environment (61) (Figs. 5D and S5C). A greater blue shift suggests deeper insertion of the peptide into the membrane and implies a higher propensity for channel formation because of interactions with the membrane's hydrophobic core (61). In contrast, smaller blue shifts indicate that the peptide mainly remains on the surface of the LUV membrane. We observed a blue shift in all the five peptides after interaction with the LUVs. However, the degree of blue shift varied between the different LUV compositions and among peptides. For example, while Amp1D exhibited a narrow range of blue shift values (–3.8 to –5.5 nm), Melittin showed a higher level of variability in values (–5.0 to –15.4 nm) (Figs. 5D and S5C). For this reason, we used hierarchical clustering analysis based on the blue shift values from each AMP (Fig. S6A). Notably, the analysis clustered AMPs with hemolytic activity (LL-37 and Melittin) separately from the AMPs without hemolytic activity (Amp1D, Seg5D, MSI-78, and 4DK5L7) (Fig. S6A). These results provide the evidence that nonhemolytic AMPs (Amp1D, Seg5D, 4DK5L7, and MSI-78) insert differently when interacting with the LUV membrane as compared with the hemolytic AMPs (Melittin and LL-37).

As a complementary approach, we investigated the interaction of Amp1D with LUVs using cryo-EM. The cryo-EM

Cholesterol-dependent mechanism of antimalarial peptides

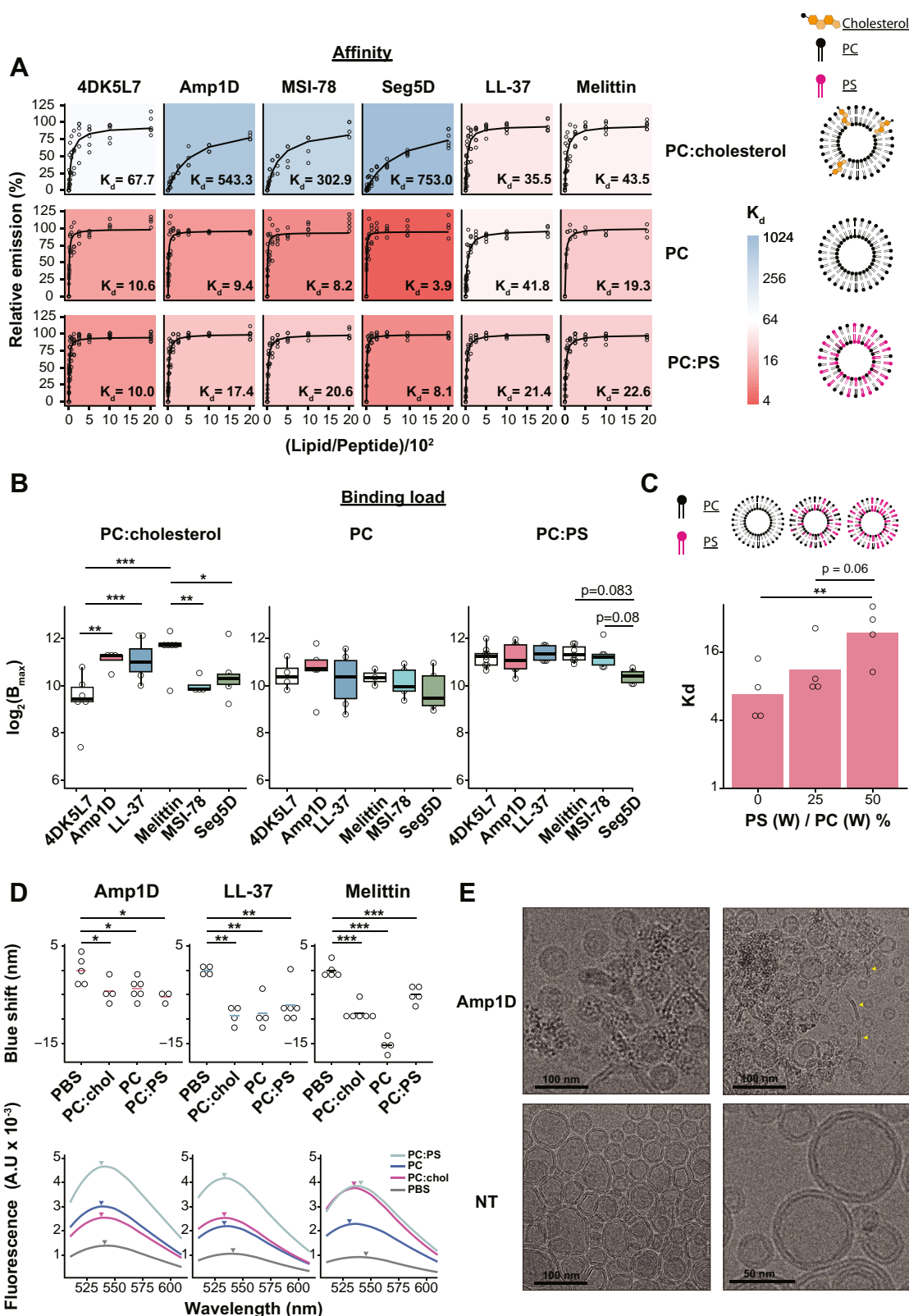


Figure 5. LUV models show AMP binding is cholesterol dependent. A and B, affinity assay using spectrofluorometer (58) of different AMPs tagged with NBD fluorophore (4DK5L7, Amp1D, LL-37, Melittin, MSI-78, and Seg5D) to LUVs. PC and PC:PS (1:1 w/w) represent the elevation levels of PS in *Pf*-IRBCs, PC:cholesterol (9:1 w/w) represents the uRBCs' membrane. The values were normalized to the best-fit maximal fluorescence (B_{max}) for each AMP and LUVs in each batch. The color code of the panels indicates the size of K_d values. Statistical analysis: The K_d and B_{max} values were obtained using the package "renz" for "R" (A). The maximal fluorescence, B_{max} , resulted from the interaction of each AMP to the different LUVs (raw values from A) [B]. Statistical analysis: Two-way ANOVA followed by Tukey's test, * $p < 0.05$, ** $p < 0.01$, and *** $p < 0.001$. C, a dose-response assay between the percentage (w/w) of PS in PC:PS LUVs (horizontal axis) and the affinity (K_d) of NBD-Amp1D to the LUVs (vertical axis). Statistical analysis: Two-way ANOVA with batch effect followed by a Tukey's test, ** $p < 0.01$. D, NBD emission blue shift of Amp1D, LL-37, and Melittin in aqueous solution (PBS) relative to NBD emission with the interaction with LUVs.

images revealed that Amp1D disrupts a fraction of the PC vesicles, resulting in the formation of small fragments (Fig. 5E). Furthermore, the addition of Amp1D induced lipid aggregation and deformation to the LUVs, causing a formation of structures resembling nanodiscs and sheets that were not observed in untreated PC LUVs (Fig. 5E). Interestingly, recent studies have shown that certain amphiphilic proteins can assemble into lipid-protein nanodiscs (62–64). In these assemblies, proteins wrap around lipid bilayer discs and reduce line tension at the bilayer edge (63, 64). These phenomena were shown also for 1-1-palmitoyl-2-oleoyl-glycero-3-phosphocholine LUVs when interacting with HNP1 and LL-37 peptides (62).

Together, our data indicate that the activity of anti-*Pf* AMPs strongly depends on the reduced levels of cholesterol within the host's RBCs during *Pf* infection. Moreover, both the binding affinity and B_{\max} levels of the LUV membranal model could serve as reliable predictors for anti-*Pf* activity and cytotoxicity of candidate AMPs.

Depleting cholesterol from uRBCs increases their susceptibility to the lytic activity of Amp1D

The results of the LUV models (Fig. 5) suggest that the high level of cholesterol in the plasma membrane protects uRBCs from Amp1D binding. To test this notion, we reduced the cholesterol level in uRBCs using methyl-beta-cyclodextrin (M β C) (65). We then exposed the treated RBCs to the labeled peptide, Rho-Amp1D (in a nonhemolytic concentration), and recorded the peptide interaction using IFC (Fig. 6, A and B).

Noticeably, upon cholesterol depletion, Rho-Amp1D was able to bind to the uRBCs in sufficient quantity to reach detectable fluorescent signals in the cells as opposed to the control (Fig. 6, A and B). Moreover, upon cholesterol depletion, Amp1D exhibited significant hemolytic activity under a nonhemolytic concentration (Fig. 6C). These results indicate that the reduced cholesterol level in the plasma membrane of the infected cell plays a central role in the preferential interaction of the D,L-KL peptide.

Discussion

Finding a long-lasting solution for malaria is a continuous challenge since the parasite rapidly develops resistance to the available drugs (2, 3), including chloroquine (66), sulfadoxine/pyrimethamine (66), and artemisinin (67). Although AMPs are extensively studied for their activity against a variety of pathogens (12, 68), less is known about their interaction with intracellular parasites, especially *Pf*. Here, we studied AMPs from the D,L-KL family as a potentially new avenue for the development of anti-*Pf* treatments. While anti-*Pf* peptides were previously reported, for example, Dermaseptin DS3 and DS4 and NK-2 (58, 69, 70), D,L KL AMPs offer additional

therapeutic advantages. The low hemolytic activity, high safety profile (22, 23, 71), and resistance to proteolytic degradation (15) suggest these AMPs can be used safely and have a sufficient lifespan in the human body to be effective against pathogens. In addition, their interaction with the membrane of *Pf* suggests that they may slow down the development of drug resistance, a critical trait when combating *Pf*.

Here, we identified two D,L-KL peptides, Amp1D and Seg5D, with anti-*Pf* activity (Fig. 1). Based on our findings, we propose key characteristics for designing new antiparasitic AMPs derived from the amphipathic parental peptides. These criteria include an optimal peptide length of approximately 15 amino acids and a relative hydrophobicity of around 55% acetonitrile (ACN). Furthermore, incorporating D-amino acids enhances anti-*Pf* activity while reducing toxicity, whereas the presence of lysine through an isopeptide bond diminishes anti-*Pf* activity. Finally, a partial or full α -helix structure with membrane interaction is recommended for effective design.

Surprisingly, other peptides of the D,L-KL family and KL peptides with isopeptide bonds were less active against *Pf* (Fig. 1). This discrepancy can be explained by the physical properties of the different peptides, and a minimum length of amino acids might be necessary to achieve anti-*Pf* activity (Fig. 1 and Table 1). Indeed, a meta-analysis of our data aligns with the previous report (72) and suggests that a critical hydrophobicity threshold exists for achieving anti-*Pf* activity (Fig. S6B). Our data also suggest that the secondary structure of AMPs likely plays a crucial role in its potency beyond just hydrophobicity. As an example, Amp1D and Seg5D share similar amino acid composition and overall hydrophobicity, Amp1D adopts partial α -helical conformation, whereas Seg5D adopts hybrid conformations, partial β -sheet, and α -helical structures in membrane-mimetic environments (14, 27). This difference in the peptide structure might contribute to the observed difference in anti-*Pf* activity (Fig. 1 and Table 1). Additional studies of the structural conformation of AMPs can contribute in determining the optimal secondary structure for anti-*Pf* activity.

We further demonstrated how Amp1D crosses the membrane of *Pf*-iRBCs, mechanically deforms it, and induces disruption in the cytoskeleton (Figs. 2–4 and S4). These results provide evidence of the NRM MoA used by Amp1D and strengthen the possibility it could be used as an anti-*Pf* drug without inducing drug resistance (15). In addition, our data indicate on the importance of cholesterol reduction in RBCs (similarly to the natural occurrences post *Pf* invasion) and in membrane mimicking LUVs, rather than the exposure of PS (Figs. 5 and 6) in mediating D,L-KL peptides' exclusive interaction with *Pf*-iRBCs. These findings are in line with previous reports showing cholesterol as the major inhibitor of AMP-membrane interaction (49) by the impediment of membrane bending (13, 73) and greater rigidity and stability, which reduces the efficacy of AMPs (13). In addition, these data are

Fluorescence emission spectra of NBD-labeled Amp1D in solution and the presence of LUVs. Statistical analysis: One-way ANOVA followed by a Dunnett's test, * $p < 0.05$, ** $p < 0.01$, *** $p < 0.001$. E, cryo-EM representative images of LUVs incubated with or without incubation of Amp1D for 1 h. Yellow arrows are examples of nanodiscs and sheets. iRBC, infected RBC; NBD, nitrobenzoxadiazole; *Pf*, *Plasmodium falciparum*; uRBC, uninfected RBC.

Cholesterol-dependent mechanism of antimalarial peptides

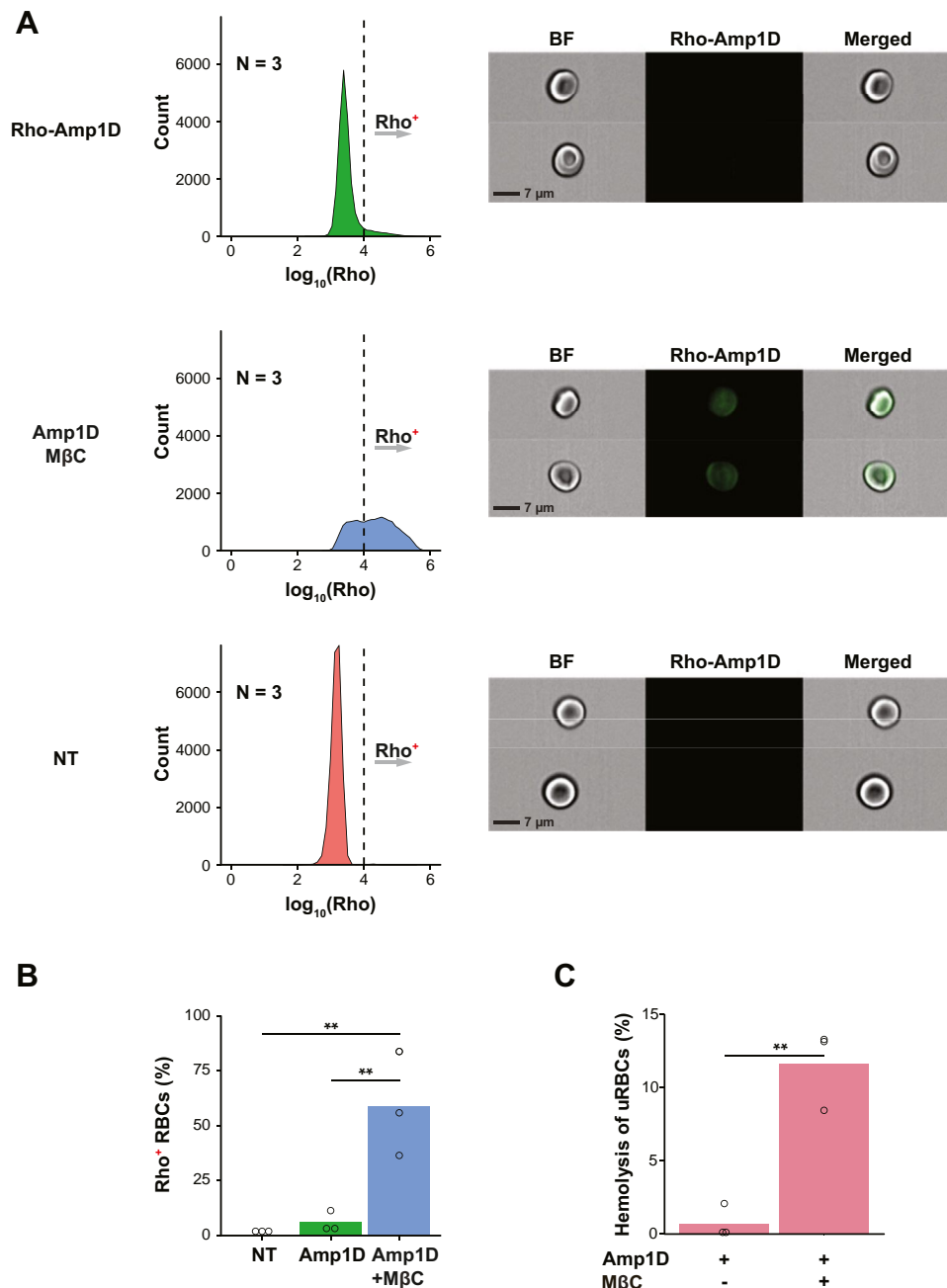


Figure 6. Cholesterol protects uRBCs from Amp1D hemolytic activity. A, binding analysis of the effect of cholesterol depletion from uRBCs on the binding to Amp1D by IFC. On the *left side*, histogram plots (N = 3) showing the fluorescence intensity of rhodamine after 30 min incubation of Rho-Amp1D with uRBCs, with or without cholesterol depletion treatment (+M β C). Based on the untreated group (NT [nontreated]), the *dashed line* marks the threshold for a positive rhodamine signal (Rho⁺). Representative IFC images, bright field (BF), rhodamine signal (Rho-Amp1D) and merged images are shown on the *right side*. B, a statistical summary of the mean percentage of Rho⁺ RBCs from (A), N = 3, one-way ANOVA followed by a Tukey's test, ****p** < 0.01. C, uRBCs were exposed to Amp1D upon treatment/mock treatment for cholesterol depletion (M β C). Hemolysis of uRBCs was measured at 1 HPT with Amp1D. Statistical analysis: *t* test, ****p** < 0.01. M β C, methyl-beta-cyclodextrin; uRBC uninfected RBC.

particularly intriguing since Amp1D signal colocalized with the enclosed parasite (Figs. 3 and S5) and its parasitic membrane, which contains higher cholesterol levels than the *Pf*-iRBC membrane (74). This unexpected result suggests that Amp1D may possess unique properties or MoA that enable it to effectively interact with the parasitic membrane despite these biophysical challenges. Deeper understanding of the interaction of AMPs and specific *Pf* proteins (75) could provide further information on the fate of the AMPs

postinternalization into *Pf*-iRBCs. Furthermore, a mice model of malaria showed a cholesterol uptake from host hepatocytes during the liver stage (76). These findings suggest that the anti-*Pf* AMPs, Amp1D and Seg5D, could potentially target *Pf* forms also during the liver stage, an asymptomatic phase of the disease. Finally, these findings pave the way for new studies on using peptides as a delivery system for antimalarial drugs. The selective activity of AMPs, particularly Amp1D, offers an approach for targeting *Pf*-iRBCs while sparing healthy cells.

The ability to differentiate between *Pf*-iRBCs and uRBCs by AMPs underpins their potential as a delivery vehicle. For example, a conjugation of Amp1D to antimalarial drugs can increase drug selectivity, maximizing drug efficacy and minimizing off-target effects (77). Moreover, combining AMPs with known antimalarial drug may result in synergistic interaction. For example, the well-studied derivative of artemisinin, dihydroartemisinin, was shown to slow down the development of the parasite from trophozoites stage to rings stage (36). Because the anti-*Pf* AMPs we study here were more active during trophozoite stage (Fig. 1E), the delay in growth post dihydroartemisinin can increase *Pf* susceptibility to AMP activity.

In summary, we provided a strong foundation for designing and using *de novo* AMPs to inhibit the growth of *Pf* parasites. The NRM MoA of Amp1D suggests that its activity can limit the ability of *Pf* to develop drug resistance. These results can be an exciting starting point for the development of a new class of anti-*Pf* AMP.

Experimental procedures

Chemical reagents and materials

All chemical reagents and materials used in this study, including their abbreviations, full names, sources, and identifiers, are listed in Table S1.

Peptide synthesis

Peptides were synthesized by an automated solid-phase peptide synthesizer (CEM Liberty Blue peptide synthesizer) on Rink Amide MBHA (100–200 mesh) resin, using the Fmoc solid-phase strategy (15). The resin-bound peptide was washed thoroughly with dimethylformamide (DMF) and dichloromethane and dried. The addition of a rhodamine fluorescent probe (Rho) to the N terminus of selected peptides was performed by standard F-moc chemistry. For the addition of NBD fluorescent labeling, resin-bound peptides were treated with NBD-Cl dissolved in DMF and 5% DIPEA, leading to the formation of resin-bound N-terminal NBD peptides. The resins were washed thoroughly with DMF and then with dichloromethane and dried under a nitrogen flow. Peptide cleavage from the resin was achieved by the addition of 95% TFA, 2.5% double-distilled water (ddH₂O), and 2.5% TIPS. The resin was filtered from the mixture, and the peptide was precipitated from the mixture using cold Et₂O. Following precipitation, the supernatant was carefully decanted, and the resulting pellet, containing the crude synthesized peptide, was obtained for further cleaning (15).

Peptide purification and purity validation

The purification of the peptides was performed by reverse-phase HPLC on an Agilent Technologies 1260 Infinity II spectrometer with a reversed-phase Vydac C₄ column at a flow rate of 1.8 ml/min and monitored with an UV detector at 215 nm. Linear gradients of 10% to 90% ACN in ddH₂O containing 0.1% TFA were used for peptide purification for 40 min. Final products were obtained by freeze-drying the collected

pure fractions. The purity of the peptides was validated with a C₁₈ reversed-phase column (Thermo Fisher Scientific; 250 mm × 4.6 mm, 5 μm particle size) at a flow rate of 0.6 ml/min using a gradient of 10% to 90% ACN in ddH₂O containing 0.1% (v/v) TFA for 40 min with UV detection at 215 nm. TOF-MS was used to determine the molecular masses of the peptides. The purity of all peptides examined for biological activity was >95%. To validate peptide synthesis, properties, and activity, in addition to synthesizing the peptide, we obtained the Amp1D peptide from custom peptide synthesis services provided by Peptide 2.0 and MSI-78 peptides from an internal services lab at the Weizmann Institute of Science.

Pf parasite culture

Pf parasites (NF54, kindly donated from the MR4 malaria source) were cultured in pooled donor RBCs provided by the Israeli Blood Bank at 4% hematocrit and incubated at 37 °C in a gas mixture of 1% O₂, 5% CO₂ in N₂ as was previously described (36). Parasites were maintained in RPMI medium, 25 mg/ml Hepes, 50 μg/ml hypoxanthine, 2 mg/ml sodium bicarbonate, 20 μg/ml gentamycin, and 0.5% Albumax II (36). Growth was monitored using methanol-fixed Giemsa-stained (Merck Millipore; catalog no.: 109203) blood smears. *Pf* cultures were tested for Mycoplasma twice a month using a MycoAlert PLUS kit.

Pf culture synchronization

Ring-stage parasites were synchronized twice a week for regular maintenance and at least once prior to experiment plating using D-sorbitol (78). Briefly, *Pf* media were removed from *Pf* cultures, and the blood pellet was incubated at 37 °C with D-sorbitol 5% solution for 5 min. Immediately after, sorbitol was removed by centrifugation, and the blood pellet was washed twice with prewarmed media.

Growth assay

Growth assays of *Pf* malaria parasites were based on a previously described method (36). Flow cytometry analysis was performed using a ZE flow cytometer (Bio-Rad) equipped with 355 and 488 nm lasers to detect infected cells based on their signal from the Hoechst-stained DNA (36, 79). Gating for *Pf*-iRBCs was based on a uRBC culture. To identify potent antimalarial peptides, a culture of 2% synchronized trophozoite *Pf*-iRBCs, 4% hematocrit, was incubated with 12.5 μM of different peptides. The culture was collected 24 HPT at the ring stage. Growth was monitored using methanol-fixed Giemsa-stained blood smears (79) and flow cytometry (36, 79). To identify the IC₅₀ values of potent antimalarial peptides, cultures of 2% synchronized trophozoite *Pf*-iRBCs 4% hematocrit were treated with increasing drug concentrations (0.19–25 μM). To compare the effect of Amp1D on rings versus trophozoite blood stage *Pf*, parasites were first synchronized and incubated at ring and trophozoite stages with 5 μM of Amp1D for 3 h. Cells were then washed and measured for the relative growth after invasion, 48 HPT and 24 HPT for rings and trophozoites, respectively, using flow cytometry.

Cholesterol-dependent mechanism of antimalarial peptides

Hemolytic activity assay

The hemolytic activity assay was carried out as previously described with the following alterations (16): Briefly, uRBCs or *Pf*-iRBCs (after isolation using magnetic column (38)) were suspended in sterile PBS (pH 7.4) at 4% hematocrit. The uRBCs or *Pf*-iRBCs were exposed to the different peptides at different concentrations (ranging from 0.19 to 25 μ M) and were incubated at 37 °C under a gas mixture of 1% O₂, 5% CO₂ in N₂. At 1 HPT and 24 HPT, the supernatant was taken out and transferred to a 96-well plate. The sample supernatant absorbance was measured at 450 nm using a microplate auto reader (SynergyMx; Biotek). uRBCs or isolated *Pf*-iRBCs were used as a negative control, and cells treated with 1% Triton X-100 were used as a positive control. The percentage of hemolysis was calculated as $([\text{sample absorbance} - \text{negative control absorbance}] / [\text{positive control absorbance} - \text{negative control absorbance}]) \times 100$ (80).

Binding selectivity and binding load analysis

Peptide binding affinity and binding load analyses were performed as previously described (60). Briefly, the binding affinity of NBD-AMPs was tracked using flow cytometry. We then compare the fraction of *Pf*-iRBCs positive to NBD from total *Pf*-iRBCs $\frac{Pf-iRBC^{+NBD}}{Pf-iRBCs\ Total}$ against the fraction of uRBCs positive to NBD from total RBCs $\frac{Naive\ RBC^{+NBD}}{Naive\ RBCs\ Total}$. In order to classify the RBC population as uRBCs or *Pf*-iRBCs, DNA-Hoechst staining was used (36). In addition, an untreated RBC sample was used as a reference to classify uRBCs and *Pf*-iRBCs as NBD positive or negative controls.

Subcellular localization of AMPs

For subcellular localization of NBD-AMPs, synchronized trophozoite-stage *Pf* parasites (2% parasitemia) were incubated with NBD-AMPs for 8 h. Parasites were stained with Hoechst for visualization of the nucleus. For subcellular localization of Rho-labeled AMPs, trophozoite-stage parasites were isolated using a magnetic column (38) and incubated with labeled AMPs for 30 min. Parasites were stained using Hoechst (2 μ M) and Rhodamine 123 (1 μ M) for visualization of the nucleus and plasma membrane (37), respectively. Cells were imaged using a multispectral IFC (ImageStreamX mark II imaging flow-cytometer; Amnis Corp, part of Cytex) as described before (81). Data were analyzed using the manufacturer's image analysis software (IDEAS 6.3; Amnis Corp). Cells were gated for focused cells, using the Gradient RMS feature and contrast, as previously described (82). Cropped cells were further eliminated by plotting the cell area of the BF image against the Centroid X feature (the number of pixels in the horizontal axis from the left corner of the image to the center of the cell mask). Then, single cells were gated, using the area and aspect ratio features. Cells positive for either NBD or rhodamine were gated by using the intensity (the sum of the background-subtracted pixel values within the masked area of the image) and the max pixel (the largest value of the background-subtracted pixel). The gate was set according to untreated cells. To quantify whether the Rho-Amp1D is

located within the nucleus, a morphology mask was created for the DNA staining (delineating the parasite nucleus) and calculated the peptide area corrected intensity within it. An additional mask was created for the rest of the parasite and RBC and calculated the peptide intensity within it. Finally, the ratio between the intensity of the peptide within the nucleus and outside it was calculated.

Atomic force microscopy

Synchronized *Pf* trophozoites (2% parasitemia) were treated with the peptide Amp1D (2.5 μ M) for 2 h. Then, using AFM, the effect of Amp1D was quantified on the height and Young's modulus of uRBCs or *Pf*-iRBCs (24). Cells were identified as uRBCs or infected based on the presence or the absence of hemozoin pigment vacuole (44, 45) in the bright field channel. Data were collected as follows: *Pf*-iRBCs in RPMI media were placed on a freshly cleaved mica surface for 5 min and rinsed with RPMI medium. AFM imaging was performed by a JPK Nanowizard III AFM microscope (Bruker Nano GmbH) in QI mode. Measurements were conducted with a qp-BioAC-CI probe (Nanosensors), with a spring constant of ≈ 0.06 N/m. In the QI mode, force-distance curves are recorded at each pixel. These are used to acquire topographic images simultaneously with nano-mechanical data. Force curves from the center of each cell were used to calculate the elastic modulus by applying the contact mechanics Hertzian model (using JPK data processing software, version 6.1.86) with a Poisson ratio of 0.5 and a conical tip shape with 22° half cone angle. For the elastic modulus measurements on the RBCs, images of 50 \times 50 μ m² were captured in 60 \times 60 pixel resolution. Images at higher resolution (20 \times 20 μ m² at 100 \times 100 pixel resolution) were also recorded to follow the differences in cell structure more precisely. The setpoint applied was 120 to 140 pN, and the approach speed was 30 μ m/s. Image analysis was performed using Gwyddion (83): an open-source software for scanning probe microscopy data analysis. JPK-scanning probe microscopy data processing software and MountainsSPII Academic (Digital Surf, version 10.0.10510).

Sample preparation for cytoskeleton AFM imaging

Freshly cleaved mica surfaces were incubated with 0.1% poly-L-lysine solution for 2 h and then rinsed with PBS. This was followed by the deposition of 100 μ l *Pf*-RBCs in PBS (10⁶ cells/ml), which was incubated for 10 min after which the cells were shear washed with 60-ml 5P8-10 buffer (5 mM Na₂HPO₄/NaH₂PO₄, 10 mM NaCl, pH 8.0) using a syringe at a $\sim 20^\circ$ angle from the surface plane. The cytoskeleton-exposed samples were dried with nitrogen flow and kept in a desiccator overnight (or longer).

AFM cytoskeleton imaging

Initial AFM imaging was carried out by using a MultiMode AFM with Nanoscope V electronics (Bruker AXS SAS) controlled with Nanoscope 9.2 software (Build R2Sr1.130547). Scans were made in PeakForce Tapping mode using a PNP-TRS, Pyrex-Nitride-probes with Silicone Nitride sensor

(NanoWorld). To locate and sample enough cells with exposed cytoskeleton for proper statistical analysis, images were collected with a fast-scan AFM system, using photothermal off-resonance tapping and small cantilevers, which fit on the base of the commercial MultiMode AFM system. The fast-scanning AFM head and control electronics were designed and built by Georg E. Fantner's group, Ecole Polytechnique Fédérale de Lausanne, Lausanne, Switzerland (84). Images were acquired by the custom LabView-based software from Georg E. Fantner's group. Scans were made with a silicon tip on a silicon nitride cantilever (Bruker FASTSCAN-C). All cytoskeleton images were analyzed using Gwyddion 2.62 software (83).

Traditional computer vision and image analysis

Two independent samples were supplied. The first sample constituted a set of 13 and 15 AFM images of untreated *Pf*-iRBCs and *Pf*-iRBCs treated with Amp1D, respectively. The second sample was composed of 14 and 10 AFM images of untreated *Pf*-iRBCs and *Pf*-iRBCs treated with Amp1D, respectively. All images were acquired by scanning the center of a cell with an exposed cytoskeleton. Each image captures a $4 \times 4 \mu\text{m}^2$ area with a resolution of 512×512 pixels. The computational pipeline was applied on two samples, independently, and composed of two parts. In the first part, the cytoskeleton backbone was segmented in each image. To achieve satisfactory segmentation, a few steps were applied. First, Gaussian blurring was applied to each image with a kernel size of 5×5 to reduce noise and make binarization more robust. Next, each image was binarized to yield the segmented backbone. For each image, a unique threshold value for binarization was calculated. To determine a unique threshold value, a pixel value distribution was obtained for each image. Then, for a shape distribution of a valley between two maxima, the threshold value was chosen as the local minima in between the two maxima. Alternatively, for a shape of distribution of maxima between two minima, a different approach was applied. The distribution was clustered to yield eight cluster centers, and then the first three cluster centers were averaged to yield a threshold for a good backbone segmentation. This enables calculating the total size of the filaments (backbone) in each image. Then, each image was inverted, so the backbone had a value of 0 and all other image features had value of 1. Contours were calculated for all image features that were not the backbone for visualization purposes. In addition, connected component analysis was applied to label the image features. This enables the calculation of the image features' area. In the second part of the pipeline, each image ($4 \times 4 \mu\text{m}^2$, 512×512 pixels) was sliced into eight \times eight images of ($0.5 \times 0.5 \mu\text{m}^2$, 64×64 pixels). Then, the mean roughness (Ra) was calculated for the sliced images. Slicing was applied to reduce the parasite crystals' effect on the image roughness and make the statistics more robust and specific to the cytoskeleton network. All pipeline calculations were fully automated.

All code was written in Python 3.9.13 (85). OpenCV library (4.9.0, <https://opencv.org/>) was applied for traditional computer vision together with Scikit-learn (1.0.2, <https://jmlr.csail.mit.edu/papers/v12/pedregosa11a.html>) and Scipy (1.9.1) (25) libraries.

LUV preparation

LUV preparation was conducted as previously described (86). Briefly, LUVs from PC, PC/PS (1:1, w/w), PC/PS (3:1, (w/w), and PC/cholesterol (9:1, w/w), which mimic the outer membranal leaflets of cholesterol depletion postparasite invasion, additional negative charge on the outer membrane of *Pf*-iRBCs and uninfected (naïve) RBCs, respectively. Lipids were dissolved in chloroform/ CH_3OH (3:1) and evaporated using nitrogen stream, followed by 3 to 24 h of vacuum pumping or lyophilization. The lipid film was then hydrated with PBS solution (osmol = 300 mOsmo/kg) to reach the desired concentration, and the solution was gently vortexed. The resulting multilamellar vesicle suspensions were sonicated for 15 min to disperse larger aggregates. The vesicles were subsequently downsized by extrusion through 1 μm , 400 nm, 200 nm, and 100 nm polycarbonate membranes. Extrusion was performed 11 times through each membrane. The liposomes' size was measured using Malvern NanoSight NS300 (nanoparticle tracking analysis) (Fig. S5A). Samples were diluted with PBS. Optimal dilution for each sample was found by pretesting the sample until an ideal particle-per-frame value (30–100 particles/frame) was obtained. For each measurement, five times 1 min videos were captured at 25 °C, with at least 300 μl displacement between each video. The number of completed tracks in nanoparticle tracking analysis measurements was always greater than the proposed minimum of 1000 to minimize data skewing based on single large particles.

AMP binding affinity to LUV assay

AMP binding affinity to LUV assay was conducted as previously described (31). Briefly, binding equilibrium (B_{max}) was determined by the varying lipid–peptide ratios, and the affinity constant was calculated from the relationship between the equilibrium emission level and lipid concentration using a steady-state affinity model. The affinity constants (K_a) were determined using a steady-state affinity model with nonlinear least squares analysis. The nonlinear least squares fitting was done using the following equation: $Y(x) = \frac{K_a \cdot X \cdot B_{\text{max}}}{1 + K_a \cdot X}$, where X is the lipid concentration, $Y(x)$ is the fluorescence emission, B_{max} is the maximal difference in the emission of peptide before and after the addition of lipids (it represents the maximum amount of peptides bound to a lipid), and K_a is the affinity constant. The accessibility of the peptides to proteolytic cleavage in the membrane-bound state was measured using proteinase K (125 $\mu\text{g}/\text{ml}$), which was added to each well to validate the insertion of the peptides into the lipid vesicles. In a control experiment, a labeled peptide was first added to the solution containing the enzyme, followed by the addition of LUVs.

Cholesterol-dependent mechanism of antimalarial peptides

NBD fluorescence measurements

The fluorescence of an NBD-labeled peptide increases upon transfer from a solution to a hydrophobic environment (31). NBD-labeled peptides were diluted in PBS to a concentration of 0.1 μM , either alone or in the presence of LUVs. LUVs were employed to minimize differential light scattering effects, maintaining a high lipid-peptide molar ratio (2000:1) to ensure negligible spectral contributions from free peptides. The fluorescence was recorded with excitation at 470 nm and an emission spectrum from 510 to 610 nm. Under these conditions, most of the peptide was bound to the vesicles.

Cryo-EM sample preparation and imaging

A sample solution of 3 μl was applied to the carbon side of lacey carbon 200 mesh copper grid (Electron Microscopy Sciences), which was glow discharged for 120 s at 0.5 mbar and 18 W with Evactron CombiClean System (XEI Scientific). Samples were blotted for 1 s from both sides at 4 $^{\circ}\text{C}$ and 100% humidity and plunged frozen into the liquid ethane cooled by liquid nitrogen using Vitrobot Mark IV (Thermo Fisher Scientific). Cryo-EM images were collected using a Talos Arctica TEM, equipped with a Falcon 4i direct detector (Thermo Fisher Scientific) and operated at 200 kV. Image acquisition was performed using Tomography 5.16 and Velox 3.8 software (Thermo Fisher Scientific) at a nominal magnification of 17.500 \times (pixel size: 1.64 nm; defocus: 10–15 μm), 45.000 \times (pixel size: 0.62 nm, defocus: 5–8 μm), or 120.000 \times (pixel size: 0.118 nm, defocus: 3–5 μm) with a total dose not exceeding 100 $\text{e}^{-}/\text{\AA}^2$.

Hemolytic activity under cholesterol depletion

uRBCs were subjected to treatment/mock treatment for cholesterol depletion using 3.12 μM of M β C for 30 min. Then, M β C was washed, and the cells were subjected to 5 μM Amp1D for 1 h (Amp1D + M β C group). The nontreated group was used as a control, as well as Amp1D (5 μM)-treated RBCs (Amp1D group), M β C-treated cells (M β C group), and a positive control group exposed to 1% Triton X-100 were collected and analyzed as explained previously under the “Hemolytic activity assay” section, with the following modification: The relative hemolysis of the Amp1D + MBC group was normalized to the M β C group, whereas the relative hemolysis of the Amp1D group was normalized to the nontreated group.

Statistical analysis

All statistical analyses performed in the present study were carried out on the mean of at least three independent biological replicates using “R” version >4 , as indicated in each figure legend. The mean of each set of biological repeats is represented in all cases. Multiple comparisons were performed where needed, as indicated in the respective figure legends, and p values were calculated to show statistical significance.

Data availability

The datasets generated during the current study are available in the public repository Zenodo: <https://doi.org/10.5281/zenodo.14577440>.

Supporting information—This article contains supporting information.

Ethics statement—Human sample studies were carried out in strict accordance with Israeli law. All samples for experiments were conducted at the Weizmann Institute of Science and approved by Israel Institutional Review Board #SMC-13-0954.

Acknowledgments—We thank the members of the N.R.R. laboratory for their support and advice, especially Dr. Ewa Kozela, Dr. Paula Karam-Cohen, Sonia Oren, Gili Mizrachi, Yuval Berger, Madeleine Egan and Dr. Anton Moisieiev for their technical assistance and insightful discussions. The graphical abstract was created in [BioRender.com](https://www.biorender.com).

Author contributions—E. K. conceptualization; E. K., D. B. H., D. A., N. A. W., M. I. M., M. G., R. K., A. D., N. E. B. Z., N. A., M. P., G. F., Z. P., I. R.-G., and C. E. C. methodology; I. A. software; E. K. and D. B. H. validation; E. K., D. B. H., R. R., Z. P., I. A., and I. R.-G. formal analysis; E. K., D. B. H., D. A., N. A. W., G. D. E., M. I. M., M. G., R. K., A. D., N. E. B. Z., I. R.-G., and C. E. C. investigation; E. K., D. B. H., and I. R.-G. data curation; E. K., D. B. H., and A. C. C. writing—original draft; E. K., D. B. H., A. C. C., Y. S., and N. R.-R. writing—review & editing; E. K., D. B. H., and A. C. C. visualization; Y. S. and N. R.-R. supervision; N.R.-R. project administration.

Funding and additional information—N. R. R. is funded by the European Union (European Research Council [ERC], MalChemAtlas, 101086598). Views and opinions expressed by the author(s) do not necessarily reflect those of the European Union or the ERC. Neither the European Union nor the granting authority can be held responsible for them. N. R. R. is supported by the Minerva Program (grant number: 714142), by the Israel Science Foundation (ISF) (grant no.: 1637/20), within the Israel Precision Medicine Partnership program and the ISF (grant application no.: 570/21) and ISF—Canada-Israel Joint Health Research Program (IDRC, CIHR, and the Azrieli Foundation) (reference number: P141807). N. R. R. is deeply grateful for the support of the Henry Chanoch Kreter Institute for Biomedical Imaging and Genomics, the Dr. Barry Sherman Institute for Medicinal Chemistry, the Karen Siem Fellowship for Women in Science, the Brenden-Mann Women’s Innovation Impact Fund and Bina, the translational research and innovation unit of the Weizmann Institute. The research of Y. S. supported by the Israeli Ministry of Science and Technology (application no.: 3-14316) and the ISF (application no.: 1944/20). N. A., M. P., and G. E. F. acknowledge funding from the European Union H2020—UE Framework Programme for Research & Innovation (2014–2020); ERC-2017-CoG; InCell; project number: 773091. N. A., M. P., and G. E. F. acknowledge funding from the European Union H2020—UE Framework Programme for Research & Innovation (2014–2020); ERC-2017-CoG; InCell; project number: 773091.

Conflict of interest—The authors declare that they have no conflicts of interest with the contents of this article.

Abbreviations—The abbreviations used are: ACN, acetonitrile; AFM, atomic force microscopy; AMP, antimicrobial peptide; ddH₂O, double-distilled water; DMF, dimethylformamide; HPT, hour post treatment; IFC, imaging flow cytometry; iRBC, infected RBC; KL, lysine and leucine residue; LUV, large unilamellar vesicle; MoA, mode of action; MβC, methyl-beta-cyclodextrin; NBD, nitrobenzoxadiazole; NRM, nonreceptor mediated; PC, phosphatidylcholine; Pf, *Plasmodium falciparum*; PS, phosphatidylserine; RBC, red blood cell; uRBC, uninfected RBC.

References

- World Health Organization (2022) *World malaria report 2022*, World Health Organization, Geneva
- Menard, D., and Dondorp, A. (2017) Antimalarial drug resistance: a threat to malaria elimination. *Cold Spring Harb Perspect. Med.* **7**, 1–24
- Sinha, S., Medhi, B., and Sehgal, R. (2014) Challenges of drug-resistant malaria. *Parasite* **21**, 61
- Phillips, M. A., Burrows, J. N., Manyando, C., Van Huijsduijnen, R. H., Van Voorhis, W. C., and Wells, T. N. C. (2017) Malaria. *Nat. Rev. Dis. Primers* **3**, 17050
- Wagner, M. P., Formaglio, P., Gorgette, O., Dziekan, J. M., Huon, C., Berneburg, I., et al. (2022) Human peroxiredoxin 6 is essential for malaria parasites and provides a host-based drug target. *Cell Rep.* **39**, 110923
- Vale, N., Moreira, R., and Gomes, P. (2009) Primaquine revisited six decades after its discovery. *Eur. J. Med. Chem.* **44**, 937–953
- Rossi, L. M., Rangasamy, P., Zhang, J., Qiu, X. Q., and Wu, G. Y. (2008) Research advances in the development of peptide antibiotics. *J. Pharm. Sci.* **97**, 1060–1070
- Mangoni, M. L., Mcdermott, A. M., and Zasloff, M. (2016) Antimicrobial peptides and wound healing: biological and therapeutic considerations. *Exp. Dermatol.* **25**, 167–173
- Biswaro, L. S., Sousa, M. G. da C., Rezende, T. M. B., Dias, S. C., and Franco, O. L. (2018) Antimicrobial peptides and nanotechnology, recent advances and challenges. *Front. Microbiol.* **9**, 855
- Oren, Z., and Shai, Y. (1998) Mode of action of linear amphipathic α -helical antimicrobial peptides. *Biopolymers* **47**, 451–463
- Zasloff, M. (2002) Antimicrobial peptides of multicellular organisms. *Nature* **415**, 389–395
- Shai, Y. (2002) Mode of action of membrane active antimicrobial peptides. *Biopolymers - Pept. Sci. Section.* **66**, 236–248
- Brender, J. R., McHenry, A. J., and Ramamoorthy, A. (2012) Does cholesterol play a role in the bacterial selectivity of antimicrobial peptides? *Front. Immunol.* **3**, 195
- Papo, N., Oren, Z., Pag, U., Sahl, H. G., and Shai, Y. (2002) The consequence of sequence alteration of an amphipathic alpha-helical antimicrobial peptide and its diastereomers. *J. Biol. Chem.* **277**, 33913–33921
- Ben Hur, D., Kapach, G., Wani, N. A., Kiper, E., Ashkenazi, M., Smollan, G., et al. (2022) Antimicrobial peptides against multidrug-resistant *Pseudomonas aeruginosa* biofilm from cystic fibrosis patients. *J. Med. Chem.* **65**, 9050–9062
- Wani, N. A., Ben Hur, D., Kapach, G., Stolovicki, E., Rotem, E., and Shai, Y. (2021) Switching bond: generation of new antimicrobial peptides via the incorporation of an intramolecular isopeptide bond. *ACS Infect. Dis.* **7**, 1702–1712
- Wani, N. A., Stolovicki, E., Hur, D. B., and Shai, Y. (2022) Site-specific isopeptide bond formation: a powerful tool for the generation of potent and nontoxic antimicrobial peptides. *J. Med. Chem.* **65**, 5085–5094
- Hallock, K. J., Lee, D. K., and Ramamoorthy, A. (2003) MSI-78, an analogue of the magainin antimicrobial peptides, disrupts lipid bilayer structure via positive curvature strain. *Biophys. J.* **84**, 3052–3060
- Chennupati, S. K., Chiu, A. G., Tamashiro, E., Banks, C. A., Cohen, M. B., Bleier, B. S., et al. (2009) Effects of an LL-37-derived antimicrobial peptide in an animal model of biofilm *Pseudomonas sinusitis*. *Am. J. Rhinol. Allergy* **23**, 46–51
- Lofton, H., Pr anting, M., Thulin, E., and Andersson, D. I. (2013) Mechanisms and fitness costs of resistance to antimicrobial peptides LL-37, CNY100HL and wheat germ histones. *PLoS One* **8**, e68875
- Yang, L., Harroun, T. A., Weiss, T. M., Ding, L., and Huang, H. W. (2001) Barrel-stave model or toroidal model? A case study on melittin pores. *Biophys. J.* **81**, 1475–1485
- Braunstein, A., Papo, N., and Shai, Y. (2004) In vitro activity and potency of an intravenously injected antimicrobial peptide and its DL amino acid analog in mice infected with bacteria. *Antimicrob. Agents Chemother.* **48**, 3127–3129
- Papo, N., Braunstein, A., Eshhar, Z., and Shai, Y. (2004) Suppression of human prostate tumor growth in mice by a cytolytic D-, L-amino Acid Peptide: membrane lysis, increased necrosis, and inhibition of prostate-specific antigen secretion. *Cancer Res.* **64**, 5779–5786
- Dekel, E., Yaffe, D., Rosenhek-Goldian, I., Ben-Nissan, G., Ofir-Birin, Y., Morandi, M. I., et al. (2021) 20S proteasomes secreted by the malaria parasite promote its growth. *Nat. Commun.* **12**, 1–19
- Virtanen, P., Gommers, R., Oliphant, T. E., Haberland, M., Reddy, T., Cournapeau, D., et al. (2020) SciPy 1.0: fundamental algorithms for scientific computing in Python. *Nat. Methods* **17**, 261–272
- Papo, N., and Shai, Y. (2005) A molecular mechanism for lipopolysaccharide protection of gram-negative bacteria from antimicrobial peptides. *J. Biol. Chem.* **280**, 10378–10387
- Segev-Zarko, L., Saar-Dover, R., Brumfeld, V., Mangoni, M. L., and Shai, Y. (2015) Mechanisms of biofilm inhibition and degradation by antimicrobial peptides. *Biochem. J.* **468**, 259–270
- Kutner, S., Ginsburg, H., and Cabantchik, Z. I. (1983) Permselectivity changes in malaria (*Plasmodium falciparum*) infected human red blood cell membranes. *J. Cell Physiol.* **114**, 245–251
- Mauritz, J. M. A., Esposito, A., Ginsburg, H., Kaminski, C. F., Tiffert, T., and Lew, V. L. (2009) The homeostasis of *Plasmodium falciparum*-infected red blood cells. *PLoS Comput. Biol.* **5**, e1000339
- Paulitschke, M., and Nash, G. B. (1993) Membrane rigidity of red blood cells parasitized by different strains of *Plasmodium falciparum*. *J. Lab. Clin. Med.* **122**, 581–589
- Saar-Dover, R., Ashkenazi, A., and Shai, Y. (2013) Peptide interaction with and insertion into membranes. *Methods Mol. Biol.* **1033**, 173–183
- Shprung, T., Wani, N. A., Wilmes, M., Mangoni, M. L., Bitler, A., Shimon, E., et al. (2021) Opposing effects of PhoPQ and PmrAB on the properties of *Salmonella enterica* serovar typhimurium: implications on resistance to antimicrobial peptides. *Biochemistry* **60**, 2943–2955
- Kapach, G., Nuri, R., Schmidt, C., Danin, A., Ferrera, S., Savidor, A., et al. (2020) Loss of the periplasmic chaperone skp and mutations in the efflux pump AcrAB-TolC play a role in acquired resistance to antimicrobial peptides in *Salmonella typhimurium*. *Front. Microbiol.* **11**, 189
- Overhage, J., Campisano, A., Bains, M., Torfs, E. C. W., Rehm, B. H. A., and Hancock, R. E. W. (2008) Human host defense peptide LL-37 prevents bacterial biofilm formation. *Infect. Immun.* **76**, 4176–4182
- Oren, Z., Lerman, J. C., Gudmundsson, G. H., Agerberth, B., and Shai, Y. (1999) Structure and organization of the human antimicrobial peptide LL-37 in phospholipid membranes: relevance to the molecular basis for its non-cell-selective activity. *Biochem. J.* **341**(Pt 3), 501–513
- Camacho, A. C., Kiper, E., Oren, S., Zaharoni, N., Nir, N., Soffer, N., et al. (2023) High-throughput analysis of the transcriptional patterns of sexual genes in malaria. *Parasit Vectors* **16**, 14
- Love, M. S., Millholland, M. G., Mishra, S., Kulkarni, S., Katie, B., Pan, W., et al. (2013) Platelet factor 4 activity against *P. falciparum* and its translation to nonpeptidic mimics as antimalarials. *Cell Host. Microbe.* **12**, 815–823
- Ribaut, C., Berry, A., Chevalley, S., Reybier, K., Morlais, I., Parzy, D., et al. (2008) Concentration and purification by magnetic separation of the erythrocytic stages of all human *Plasmodium* species. *Malar. J.* **7**, 45
- Amaro, M., Filipe, H. A. L., Prates Ramalho, J. P., Hof, M., and Loura, L. M. S. (2016) Fluorescence of nitrobenzoxadiazole (NBD)-labeled lipids in model membranes is connected not to lipid mobility but to probe location. *Phys. Chem. Chem. Phys.* **18**, 7042–7054

Cholesterol-dependent mechanism of antimalarial peptides

40. Shmuel-Galia, L., Klug, Y., Porat, Z., Charni, M., Zarmi, B., and Shai, Y. (2017) Intramembrane attenuation of the TLR4-TLR6 dimer impairs receptor assembly and reduces microglia-mediated neurodegeneration. *J. Biol. Chem.* **292**, 13415–13427
41. Papo, N., Shahar, M., Eisenbach, L., and Shai, Y. (2003) A novel lytic peptide composed of DL-amino acids selectively kills cancer cells in culture and in mice. *J. Biol. Chem.* **278**, 21018–21023
42. Cohen, H., Wani, N. A., Ben Hur, D., Migliolo, L., Cardoso, M. H., Porat, Z., et al. (2023) Interaction of pexiganan (MSI-78)-Derived analogues reduces inflammation and TLR4-mediated cytokine secretion: a comparative study. *ACS Omega* **8**, 17856–17868
43. Flammersfeld, A., Lang, C., Flieger, A., and Pradel, G. (2018) Phospholipases during membrane dynamics in malaria parasites. *Int. J. Med. Microbiol.* **308**, 129–141
44. Jackson, K. E., Klonis, N., Ferguson, D. J. P., Adisa, A., Dogovski, C., and Tilley, L. (2004) Food vacuole-associated lipid bodies and heterogeneous lipid environments in the malaria parasite, *Plasmodium falciparum*. *Mol. Microbiol.* **54**, 109–122
45. Wongtanachai, J., Silamut, K., Day, N. P. J., Dondorp, A., and Chaisri, U. (2012) Effects of antimalarial drugs on movement of *Plasmodium falciparum*. *Southeast Asian J. Trop. Med. Public Health* **43**, 1–9
46. Millholland, M. G., Chandramohanadas, R., Pizzarro, A., Wehr, A., Shi, H., Darling, C., et al. (2011) The malaria parasite progressively dismantles the host erythrocyte cytoskeleton for efficient egress. *Mol. Cell Proteomics* **10**, M111.010678
47. Sinha, A., Chu, T. T. T., Dao, M., and Chandramohanadas, R. (2015) Single-cell evaluation of red blood cell bio-mechanical and nano-structural alterations upon chemically induced oxidative stress. *Sci. Rep.* **5**, 9768
48. Li, J., Lykotraftitis, G., Dao, M., and Suresh, S. (2007) Cytoskeletal dynamics of human erythrocyte. *Proc. Natl. Acad. Sci. U. S. A.* **104**, 4937–4942
49. Vale, N., Aguiar, L., and Gomes, P. (2014) Antimicrobial peptides: a new class of antimalarial drugs? *Front. Pharmacol.* **5**, 275
50. Brown, A. C., Moore, C. C., and Guler, J. L. (2020) Cholesterol-dependent enrichment of understudied erythrocytic stages of human *Plasmodium* parasites. *Sci. Rep.* **10**, 1–15
51. Maguire, P. A., Prudhomme, J., and Sherman, I. W. (1991) Alterations in erythrocyte membrane phospholipid organization due to the intracellular growth of the human malaria parasite, *Plasmodium falciparum*. *Parasitology* **102**, 179–186
52. Kaushik, N. K., Sharma, J., and Sahal, D. (2012) Anti-plasmodial action of de novo-designed, cationic, lysine-branched, amphipathic, helical peptides. *Malar. J.* **11**, 256
53. Sam-Yellowe, T. Y., Perkins, M. E., and Interaction, M. E. (1991) Interaction of the 140/130/110 kDa Rhoptyry Protein Complex *Plasmodium falciparum* with the Erythrocyte Membrane and Liposomes Erythrocyte invasion by the malarial parasite is a multistep process involving sequential events: surface attachment, m. *Exp. Parasitol.* **171**, 161–171
54. Ashkenazi, A., Faingold, O., Kaushansky, N., Ben-Nun, A., and Shai, Y. (2013) A highly conserved sequence associated with the HIV gp41 loop region is an immunomodulator of antigen-specific T cells in mice. *Blood* **121**, 2244–2252
55. Gazit, E., and Shai, Y. (1993) Structural characterization, membrane interaction, and specific assembly within phospholipid membranes of hydrophobic segments from *Bacillus thuringiensis* var. israelensis cytolytic toxin. *Biochemistry* **32**, 12363–12371
56. Hiratsuka, T., and Kato, T. (1987) A fluorescent analog of colcemid, N-(7-nitrobenz-2-oxa-1,3-diazol-4-yl)-colcemid, as a probe for the colcemid-binding sites of tubulin and microtubules. *J. Biol. Chem.* **262**, 6318–6322
57. Makovitzki, A., Avrahami, D., and Shai, Y. (2006) Ultrashort antibacterial and antifungal lipopeptides. *Proc. Natl. Acad. Sci. U. S. A.* **103**, 15997–16002
58. Ghosh, J. K., Shaool, D., Guillaud, P., Cicéron, L., Mazier, D., Kustanovich, I., et al. (1997) Selective cytotoxicity of dermaseptin S3 toward intraerythrocytic *Plasmodium falciparum* and the underlying molecular basis. *J. Biol. Chem.* **272**, 31609–31616
59. Hernández-Castañeda, M. A., Lavergne, M., Casanova, P., Nydegger, B., Merten, C., Subramanian, B. Y., et al. (2021) A profound membrane reorganization defines susceptibility of *Plasmodium falciparum* infected red blood cells to lysis by granulysin and perforin. *Front. Immunol.* **12**, 643746
60. Fink, A., Ben Hur, D., Wani, N. A., Cohen, H., Segev-Zarko, L.-A., Arnusch, C. J., et al. (2024) Development of nontoxic peptides for lipopolysaccharide neutralization and sepsis treatment. *ACS Pharmacol. Transl. Sci.* **7**, 1795–1806
61. Shai, Y. (1999) Mechanism of the binding, insertion and destabilization of phospholipid bilayer membranes by α -helical antimicrobial and cell non-selective membrane-lytic peptides. *Biochim. Biophys. Acta Biomembr.* **1462**, 55–70
62. Drab, E., and Sugihara, K. (2020) Cooperative function of LL-37 and HNP1 protects mammalian cell membranes from lysis. *Biophys. J.* **119**, 2440–2450
63. Denisov, I. G., Grinkova, Y. V., Lazarides, A. A., and Sligar, S. G. (2004) Directed self-assembly of monodisperse phospholipid bilayer nanodiscs with controlled size. *J. Am. Chem. Soc.* **126**, 3477–3487
64. Xu, X. P., Zhai, D., Kim, E., Swift, M., Reed, J. C., Volkmann, N., et al. (2013) Three-dimensional structure of Bax-mediated pores in membrane bilayers. *Cell Death Dis.* **4**, e683
65. Ahiya, A. I., Bhatnagar, S., Morrissey, J. M., Beck, J. R., and Vaidya, A. B. (2022) Dramatic consequences of reducing erythrocyte membrane cholesterol on *Plasmodium falciparum*. *Microbiol. Spectr.* **10**, e0015822
66. Mita, T., Tanabe, K., and Kita, K. (2009) Spread and evolution of *Plasmodium falciparum* drug resistance. *Parasitol. Int.* **58**, 201–209
67. Wongsrichanalai, C., and Sibley, C. H. (2013) Fighting drug-resistant *Plasmodium falciparum*: the challenge of artemisinin resistance. *Clin. Microbiol. Infect.* **19**, 908–916
68. Mangoni, M. L., Saugar, J. M., Dellisanti, M., Barra, D., Simmaco, M., and Rivas, L. (2005) Temporins, small antimicrobial peptides with leishmanicidal activity. *J. Biol. Chem.* **280**, 984–990
69. Gelhaus, C., Jacobs, T., Andrä, J., and Leippe, M. (2008) The antimicrobial peptide NK-2, the core region of mammalian NK-lysin, kills intraerythrocytic *Plasmodium falciparum*. *Antimicrob. Agents Chemother.* **52**, 1713–1720
70. Mor, A. (2009) Multifunctional host defense peptides: antiparasitic activities. *FEBS J.* **276**, 6474–6482
71. Papo, N., Seger, D., Makovitzki, A., Kalchenko, V., Eshhar, Z., Degani, H., et al. (2006) Inhibition of tumor growth and elimination of multiple metastases in human prostate and breast xenografts by systemic inoculation of a host defense-like lytic peptide. *Cancer Res.* **66**, 5371–5378
72. Gagnon, M. C., Strandberg, E., Grau-Campistany, A., Wadhwani, P., Reichert, J., Bürck, J., et al. (2017) Influence of the length and charge on the activity of α -helical amphipathic antimicrobial peptides. *Biochemistry* **56**, 1680–1695
73. Papo, N., and Shai, Y. (2004) Effect of drastic sequence alteration and D-amino acid incorporation on the membrane binding behavior of lytic peptides. *Biochemistry* **43**, 6393–6403
74. Maier, A. G., and van Ooij, C. (2022) The role of cholesterol in invasion and growth of malaria parasites. *Front. Cell Infect. Microbiol.* **12**, 984049
75. Mardirossian, M., Grzela, R., Giglione, C., Meinel, T., Gennaro, R., Mergaert, P., et al. (2014) The host antimicrobial peptide Bac71-35 binds to bacterial ribosomal proteins and inhibits protein synthesis. *Chem. Biol.* **21**, 1639–1647
76. Bano, N., Romano, J. D., Jayabalasingham, B., and Coppens, I. (2007) Cellular interactions of *Plasmodium* liver stage with its host mammalian cell. *Int. J. Parasitol.* **37**, 1329–1341

77. Zhang, X., Wang, M., Zhu, X., Peng, Y., Fu, T., Hu, C. H., *et al.* (2022) Development of lipo-?-AA peptides as potent antifungal agents. *J. Med. Chem.* **65**, 8029–8039
78. Lambros, C., and Vandenberg, J. P. (1979) Synchronization of *Plasmodium falciparum* erythrocytic stages in culture. *J. Parasitol.* **65**, 418–420
79. Dekel, E., Rivkin, A., Heidenreich, M., Nadav, Y., Ofir-Birin, Y., Porat, Z., *et al.* (2017) Identification and classification of the malaria parasite blood developmental stages, using imaging flow cytometry. *Methods* **112**, 157–166
80. Grieco, P., Carotenuto, A., Auriemma, L., Saviello, M. R., Campiglia, P., Gomez-Monterrey, I. M., *et al.* (2013) The effect of d-amino acid substitution on the selectivity of temporin L towards target cells: identification of a potent anti-*Candida* peptide. *Biochim. Biophys. Acta. Biomembr.* **1828**, 652–660
81. Alfandari, D., Ben Ami Pilo, H., Abou Karam, P., Dagan, O., Joubran, C., Rotkopf, R., *et al.* (2022) Monitoring distribution dynamics of EV RNA cargo within recipient monocytes and macrophages. *Front. Cell Infect. Microbiol.* **11**, 739628
82. Fendl, B., Weiss, R., Fischer, M. B., Spittler, A., and Weber, V. (2016) Characterization of extracellular vesicles in whole blood: influence of pre-analytical parameters and visualization of vesicle-cell interactions using imaging flow cytometry. *Biochem. Biophys. Res. Commun.* **478**, 168–173
83. Nečas, D., and Klapetek, P. (2012) Gwyddion: an open-source software for SPM data analysis. *Cent. Eur. J. Phys.* **10**, 181–188
84. Nievergelt, A. P., Banterle, N., Andany, S. H., Gönczy, P., and Fantner, G. E. (2018) High-speed photothermal off-resonance atomic force microscopy reveals assembly routes of centriolar scaffold protein SAS-6. *Nat. Nanotechnol.* **13**, 696–701
85. Van Rossum, G (2010) *The Python language reference. Release 3.0.1 [Repr.]*. Python Software Foundation, Hampton, NH, Redwood City, CA. SoHo Books (Documentation for Python, Pt. 2)
86. Rotem, E., Reuven, E. M., Klug, Y. A., and Shai, Y. (2016) The transmembrane domain of HIV-1 gp41 inhibits T-cell activation by targeting multiple T-cell receptor complex components through its GxxxG motif. *Biochemistry* **55**, 1049–1057